Thermoplastic nanofluidic devices for biomedical applications

Kumuditha M. Weerakoon-Ratnayake,†[ae] Colleen E. O'Neil,†[be] Franklin I. Uba†[b] and Steven A. Soper*[cdef]

Microfluidics is now moving into a developmental stage where basic discoveries are being transitioned into the commercial sector so that these discoveries can affect, for example, healthcare. Thus, high production rate microfabrication technologies, such as thermal embossing and/or injection molding, are being used to produce low-cost consumables appropriate for commercial applications. Based on recent reports, it is clear that nanofluidics offers some attractive process capabilities that may provide unique venues for bio-molecular analyses that cannot be realized at the microscale. Thus, it would be attractive to consider early in the developmental cycle of nanofluidics production pipelines that can generate devices possessing sub-150 nm dimensions in a high production mode and at low-cost to accommodate the commercialization of this exciting technology. Recently, functional sub-150 nm thermoplastic nanofluidic devices have been reported that can provide high process yield rates, which can enable commercial translation of nano-fluidics. This review presents an overview of recent advancements in the fabrication, assembly, surface modification and the characterization of thermoplastic nanofluidic devices. Also, several examples in which nanoscale phenomena have been exploited for the analysis of biomolecules are highlighted. Lastly, some general conclusions and future outlooks are presented.

Introduction

Nanofluidic devices have become an ideal platform for investigating fundamental physical and chemical phenomena that are not readily accessible at the microscale. These include concentration polarization,[1–3] nonlinear electrokinetic flow and ion focusing,[4,5] mass transport in geometrically confined spaces,[6,7] nanocapillarity,[8] and electrical double layer (EDL) overlap effects.[1,9–11] Interestingly, these phenomena can also be used to carry out unique processing capabilities to enable bioassays that cannot be realized using microfluidics.

Early nano-based experiments utilized nanopores – structures whose depth is comparable to its diameter – as platforms for studying the transport properties of ions or molecules in confined space and the analysis of biomolecules.[12–19] Recently, nanofluidic devices with one or two dimensions in the nanometer scale, nanoslits or nanochannels, respectively, are being used for a number of applications due to their flexibility in terms of shape and size with surface properties that can be tuned to accommodate the required function.[20,21]

Because of the unique properties that arise when the channel size is comparable to either the length scale of electrostatic interactions in solution or the size of the molecules being transported through them, nanochannel-based devices have garnered attention for applications such as single-molecule analyses,[17,22–24] molecular pre-concentration,[5] chemical analyses of mass-limited samples,[4,25] DNA electrophoresis,[26–28] desalination,[29] nanofluidic diodes,[30] real-time probing of biomolecules,[31–35] ion transport,[36] entropic trapping for DNA separations,[37] electrophoretic separations,[37,38] manipulation of single molecules,[39] and control of molecular transport and wall interactions.[40,41]

For several years, inorganic-based substrates, such as silicon, glass or fused silica, were commonly used for nanofluidics. Glass possesses well-established surface chemistry, hydrophilic surfaces allowing for favorable wetting when using aqueous solvents, good insulating properties, minimal surface defects, non-deformability at high pressures and well-established top-down fabrication techniques.[42,43] However, the challenge with the use of inorganic substrates for

[a] Department of Biomedical Engineering, University of North Carolina, Chapel Hill, NC 27599, USA
[b] Department of Chemistry, University of North Carolina at Chapel Hill, Chapel Hill, NC 27599, USA
[c] Department of Chemistry and Department of Mechanical Engineering, University of Kansas, Lawrence, KS 66047, USA. E-mail: ssoper@ku.edu; Tel: +1 (785) 864 3072
[d] Kansas University Medical Center NIH Cancer Center, Kansas City, KS 66106, USA
[e] NIH Biotechnology Resource Center of Biomodular Multiscale Systems for Precision Medicine, USA
[f] Ulsan National Institute of Science and Technology, Ulsan, South Korea
† These authors contributed equally to this work.

nanofluidics is the sophisticated, and high-cost fabrication technologies required to make devices.

Recently, thermoplastics such as poly(methylmethacrylate), PMMA, polycarbonate, PC, cyclic olefin copolymer, COC, and polyethylene terephthalate, PET, have become viable substrates for fluidic applications, especially microfluidics. The use of thermoplastics is attractive due to the diverse and simple fabrication techniques that can be employed to produce devices in a high production mode and at low-cost using such techniques as injection molding or hot embossing.[44-46] Even nanofluidic devices can take advantage of high production mode fabrication technologies to produce the relevant

devices, which includes nanoimprint lithography (NIL) or compression injection molding.[47-49] These replication-based technologies have the potential to produce devices in high production modes and at low cost.[50-53] In addition, thermoplastics' diverse physiochemical properties and the availability of a wide range of simple activation techniques can be employed to generate surface-confined functional groups[54-58] to produce surfaces to accommodate the intended application.

In spite of the various fabrication techniques available for producing nanochannels in thermoplastics, it is not until recently that thermoplastics are being adopted as substrates for nanofluidics. The slow evolution of these devices have

Kumuditha M. Weerakoon Ratnayake

Dr. Kumuditha M. Weerakoon Ratnayake is a postdoctoral researcher within the Biomedical Engineering Department at the University of North Carolina – Chapel Hill. He received his Ph. D. in Chemistry from Louisiana State University, Baton Rouge in 2015 and his BS in Computational Chemistry (2008) from University of Colombo, Sri Lanka. His current research involves developing an automated fluorescent in situ hybridization (FISH) imaging microfluidic system and DNA damage site detection induced by chemotherapy from cancer patients using nanofluidic devices. His research interests include medical device development, point-of-care diagnostics and cancer prognosis using microfluidics/nanofluidics.
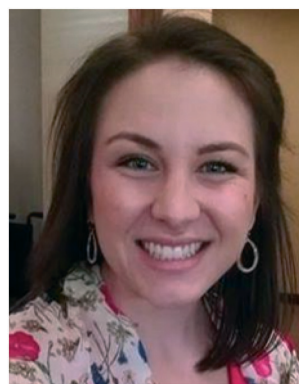
Colleen E. O'Neil

Dr. Colleen O'Neil graduated from the University of North Carolina at Chapel Hill under the advisement of Dr. Steven A. Soper. Her work focused on the development of a thermoplastic nanofluidic sensor utilizing a time-of-flight detection modality for various applications, including DNA sequencing. Furthermore, she investigated phenomenon unique to the use of thermoplastic materials on the nanoscale such as stick/slip motion, EOF fluid flow profiles and non-homogenous thermoplastic surfaces. Prior to her appointment at UNC, she received her BA from St. Mary's College of Maryland in Biochemistry.

Franklin I. Uba

Franklin Uba received his B.Sc. in Industrial Chemistry (First Class honors) from the University of Ibadan, Nigeria in 2007 and an M.S. in Chemistry from Louisiana State University in 2011. In 2014, he received a PhD in Chemistry from The University of North Carolina at Chapel Hill with his research work focusing on the development of nanofluidic devices for single-molecule DNA diagnostics. During his PhD work, he was a visiting researcher at Ulsan National Institute of Science and Technology (UNIST), South Korea. He is currently a Scientist in the Technology Research and Development division of Phillips 66 Company.

Steven A. Soper

Prof. Soper is currently a Foundation Distinguished Professor in Chemistry and Mechanical Engineering at the University of Kansas and holds an appointment at Ulsan National Institute of Science and Technology in South Korea. Soper received his Ph.D. from the University of Kansas in 1989 followed by a Postdoctoral Fellowship at Los Alamos National Laboratory, where he worked on single-molecule detection. He was at LSU within the Department of Chemistry until 2011, where he filled the Pryor Chair of Chemistry and from 2011–2016 was at UNC-Chapel Hill. Soper founded the Center of BioModular Multi-Scale Systems for Precision Medicine, which seeks to develop transformative tools for making health-related measurements.

been due to challenges associated with channel deformation and collapse encountered during device assembly – sealing a cover plate to the patterned fluidic substrate – and insufficient understanding of surface charge effects on the transport properties of molecules through thermoplastic nanochannels. In this review, we describe basic phenomena associated with the use of nanochannels for molecular assays, the fabrication of nanofluidic devices using thermoplastic substrates, assembly of nanofluidic devices, and several applications for the analysis of biomolecules using nanofluidic devices.

Scaling effects on nanoscale transport

While microfluidics involves flow in channels with dimensions >150 nm, nanofluidics entails flow in slits with at least one dimension (channels = two dimensions) ranging from 1 to 150 nm.[59] A distinct feature of nanofluidics is that the relevant length scale is comparable to the range of surface and interfacial forces in liquids, such as electrostatic, van der Waals and steric interactions. As the dimensions of fluidic devices approach the nanoscale, changes in the dominating forces as well as the physics of the processes for fluid/particle transport diverge from what is typically seen in channels with dimensions >150 nm.[60,61]

Transport processes unique to the nanoscale arise from an increase in the surface-to-volume ratio of the channel.[60,61] Consequently, forces resulting from pressure, inertia, viscosity or gravity that usually play a dominant role in microscale flows become less dominate in nanofluidic devices while interfacial forces such as surface tension, become dominant. Conlisk et al.[61] discussed the pressure drop (Δp) and applied potential (V) for driving flow as a function of channel height for a nano-slit (Fig. 1). As the channel height is reduced from 80 nm to 10 nm and for a flow-rate of 1 µL min⁻¹, the pressure drop in-

Fig. 1 Required pressure drop and voltage drop for nanochannels with different channel heights. Nanochannel length and width are 3.5 µm and 2.3 µm, respectively; zeta potential is −11 mV for 1 M NaCl solution. Reproduced from Conlisk et al., Electrophoresis, 2005, **26**, 1896–1912. Insert shows the comparison between the parabolic and plug flow profiles from the pressure-driven and electroosmotic flow, respectively.

creases from 0.006 to 3 atm (~50 000% increase), while the voltage required to maintain this same volume flow rate increases by ~560% (0.05 V to 0.33 V). Therefore, it becomes difficult to transport fluids in nanoscale systems via pressure driven flow and easier to utilize electrokinetic (EK) flow.

Because the reduction in channel size increases the surface-to-volume ratio, surface reactions are prevalent and surface roughness gradually begins to contribute to the overall flow dynamics.[4,7,62–66] Previous theories on EK flow in microchannels utilizing Boltzmann distributions and the Poisson–Boltzmann equation cannot be directly applied to nanochannels because the concentration of co- and counter ions in nanochannels are unequal due to partial overlap in the electrical double layer (EDL).[65] This requires the development of new theories to explain EK flows in nanochannels. Furthermore, relevant theories are required to explain EK flow within thermoplastic nanochannels due to the non-uniformity of surface charge arising from their amorphous nature.[67]

At the nanoscale, the EDL leads to non-uniformity in the motion of the bulk solvent as well as non-uniform transverse electric fields resulting in Poiseuille-like flow.[4,62,64,66] This non-uniformity has effects on separations within nanochannels due to the fact that analytes spend a significant time migrating through the EDL.[64] Counterions are more attracted to the wall and their flow is impeded due to no-slip flow, while co-ions are repelled from the wall and are thus, transported faster.[4,62] In addition, differences in flow based on size can be observed in nanofluidic channels because smaller molecules approach the wall to a greater degree and experience slower velocities compared to larger molecules.[4] Also, at the nanometer scale, the kinetics of adsorption/desorption approach the time required for diffusion forcing considerations of wall effects.[64]

Furthermore, concentration polarization can be observed at the interface between microchannels and nanochannels due to the increased flux of ions in the nanochannel resulting from the perturbed transport of selected ions within the EDL.[4,62,64] When the EDL spans the dimensions of the nanochannel, counterions are able to pass through the channel while co-ions are excluded resulting in the accumulation of co-ions at the inlet of the nanochannel with an increased transport of counterions.

Lower velocities may also be observed within nanochannels when compared to microchannels due to EDL overlap[62] and electro-viscosity effects.[62,68–70] The decrease in channel dimensions can cause the ratio of the apparent to true viscosities to become as high as 1.3 depending on the material of the channel wall, spatial size and shape of the channel, ionic concentration, zeta potential, temperature, dielectric constant and other properties associated with the liquid. This increase in viscosity can result in an apparent decrease in the electroosmotic flow (EOF) within nanochannels.[69]

Flow in thermoplastic nanochannels

Most fluid dynamics simulations involving nanoscale transport assumes a uniform surface chemistry, for example a fused silica substrate that is highly ordered due to its
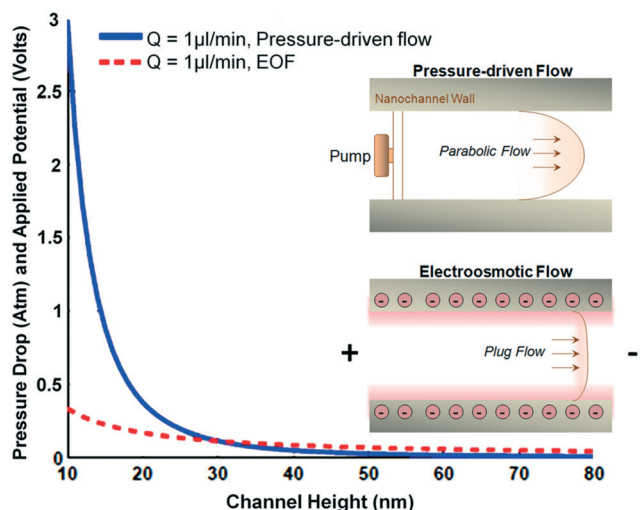
crystalline nature. Thermoplastics, however, are amorphous in structure and may have non-uniform surface chemistry. Due to the high surface area to volume ratio associated with nano domains and the small length scale, continuum theories are limited in their predictions, especially when taking into account the random nature of the surface chemistry associated with thermoplastics. Thus, molecular dynamics (MD) simulations are required to explain the fluid dynamics at the nanoscale. For example, MD simulation studies by Moldovan and co-workers explored nanofluidic systems with smooth and rough Lennard-Jones walls using both gravity and electrokinetic flow.[71,72] According to their findings, there was a difference in the adsorption/desorption times of deoxynucleotide monophosphates (dNMPs), which allowed separation of these molecules based upon their molecular dependent adsorption/desorption characteristics. One study[72] suggested the potential to separate dNMPs based on their molecular dependent electrokinetic transport properties in nanochannels arising from the chemical inhomogeneity of the channel walls when using high field strengths. The presence of high surface-to-volume ratios associated with nanochannels provided efficient heat dissipation when using high electric fields for the separation. The authors further suggested the use of Brownian dynamics (BD),[73] which involve the calculation of potential mean forces (PMFs) between the dNMPs and the channel wall in 3-dimensions.

In a recent report, O'Neil et al. showed that non-uniform charged surfaces resulting from surface activation (UV/O_3 or O_2 plasma exposure of the thermoplastic surface) can lead to electrokinetic velocities that are both positive and negative (i.e., recirculation).[67] However, this study used COMSOL Multiphysics, a continuum flow based model, to simulate the experimental results, which does not fully model the fluid dynamics at the nanoscale.

Fabrication of nanofluidic devices

Several reviews have discussed different techniques for the fabrication of nanofluidic devices.[74–79] As such, in this review we will only briefly introduce some common fabrication modalities used for creating nanofluidic slits or channels. For the most part, the fabrication technique adopted depends on the substrate of choice, which may be inorganic (fused silica, glass, silicon nitride or silicon) or organic (elastomers or thermoplastics), and the desired dimension of the nanostructures. For this review, we will only briefly discuss fabrication modalities in inorganic substrates, such as glass, to serve as a comparison to thermoplastic nanofluidic devices. We will not review device fabrication techniques for elastomeric-based devices.

Fabricating nanofluidic devices in inorganic substrates

Inorganic substrates have been widely used as substrates for nanofluidic devices due to their established surface chemistry, excellent optical properties and well-entrenched fabrication techniques.[76] Prominent techniques for the fabrication of nanochannels in inorganic substrates utilize a top-down

approach with direct writing via electron beam lithography (EBL) followed by etching or focused ion beam (FIB) milling. Over the years, several research groups have utilized EBL and/or FIB to develop nanofluidic devices in inorganic substrates for the analysis of biomolecules or evaluating transport properties in nanofluidic channels.[24,28,35,80,81]

Other techniques for making nanofluidic devices in inorganic substrates include the use of nanowires as sacrificial templates,[82] conventional machining by etching of a sacrificial strip separating a substrate and the capping layer[42] and self-enclosing of nanochannels using a UV laser pulse.[53] A relatively new technique for the direct writing of sub-10 nm structures into Si or other inorganic substrates is He ion beam writing.[83,84] In this case, low atomic mass He ions are used instead of Ga ions with the concomitant less scattering of He ions with respect to Ga ions resulting in the ability to form nanostructures with much smaller dimensions.

The challenge with using inorganic substrates is the fact that EBL or FIB must be used, in many cases, to make each device thus prohibiting the use of nanofluidic devices for most applications based on the cost of producing the device. While a commercial entity does market glass or silicon-based nanofluidic devices using deep UV lithography, the structure size is limited to around 50 nm and the device cost is high (www.bionanogenomics.com). Thus, alternative fabrication strategies must be considered to realize better accessibility of nanofluidic devices into the general research and commercial sectors, especially in the diagnostic regime where disposable devices are required due to issues arising from cross-contamination giving rise to false positive results.

Fabrication of thermoplastic nanofluidic devices

Thermoplastics are high molecular weight, linear or branched polymers with a higher Young's modulus and a wider range of physicochemical properties compared to the elastomer, PDMS. The deformability of thermoplastics makes them useful substrates for the fabrication of microfluidic channels via hot embossing, injection molding, compression molding, thermal forming or casting. Typical thermoplastics, including PMMA, PC, COC and PET, possess glass transition temperatures (T_g) that are significantly lower than that of glass allowing for the fabrication of nanostructures at high production rates, low cost and high fidelity using techniques such as NIL. Furthermore, copolymers can be used as substrates for nanofluidic devices that have a range of physiochemical properties arising from differences in the ratio of monomeric components used in them.[85]

Since its first report in the 1990s,[86–88] NIL has been used for the production of nanochannels in thermoplastics and has demonstrated production of sub-10 nm structures. The main advantage of NIL is the ability to build multi-scale patterns in a single imprinting step. Further details on NIL is presented in a recent review by Chantiwas et al.[76]

Additional techniques for the fabrication of nanochannels in thermoplastics includes direct proton beam writing,[89] thermomechanical deformation,[90] compression of

microchannels,[91] sidewall lithography and hot embossing,[92] UV-lithography/O_2 plasma etching,[93] hot embossing with PMMA molds,[94] refill of polymer microchannels,[95] and the use of silica nanowire templates.[96]

For NIL-based fabrication of nanofluidic devices, the process begins by patterning access microchannels into a Si substrate using conventional optical lithography (see Fig. 2A).[97] This is followed by FIB milling of nanochannels into the same Si substrate containing the microchannels. This Si wafer is then used as a mold master, which has the same polarity as the desired thermoplastic device. Once the Si mold master is produced, UV-NIL is undertaken to produce resin stamps with the reverse polarity as the thermoplastic device. These resin stamps are then used in a thermal-NIL step to generate the finished thermoplastic device. The advantage of this production process is that a number of nanofluidic devices (>100) can be produced from the same Si master without requiring to return to the optical lithography and FIB patterning tools, significantly reducing the cost of generating nanofluidic devices.

Assembly of thermoplastic nanofluidic devices

The aforementioned techniques for producing nanostructures in thermoplastics employ a top-down approach and as such, an assembly step is required to enclose the fluidic network. Table 1 outlines literature associated with fabricating thermoplastic nanofluidic devices and the bonding method used to assemble the device. Bonding methods include solvent-assisted bonding, thermal bonding and PDMS sealing, for example. Sealing the device with a cover plate must ensure a strong bond between the substrate and cover plate as well as high integrity of the nanostructures following assembly. When working with thermoplastic substrates several parameters must be considered when determining the best sealing methodology, including the polymer solubility and the Hildebrand parameter, the surface energy and roughness as well as the plastic's T_g.

Solvent bonding of thermoplastics takes advantage of the polymer's solubility to entangle polymer chains at the point of contact between the substrate and cover plate. The
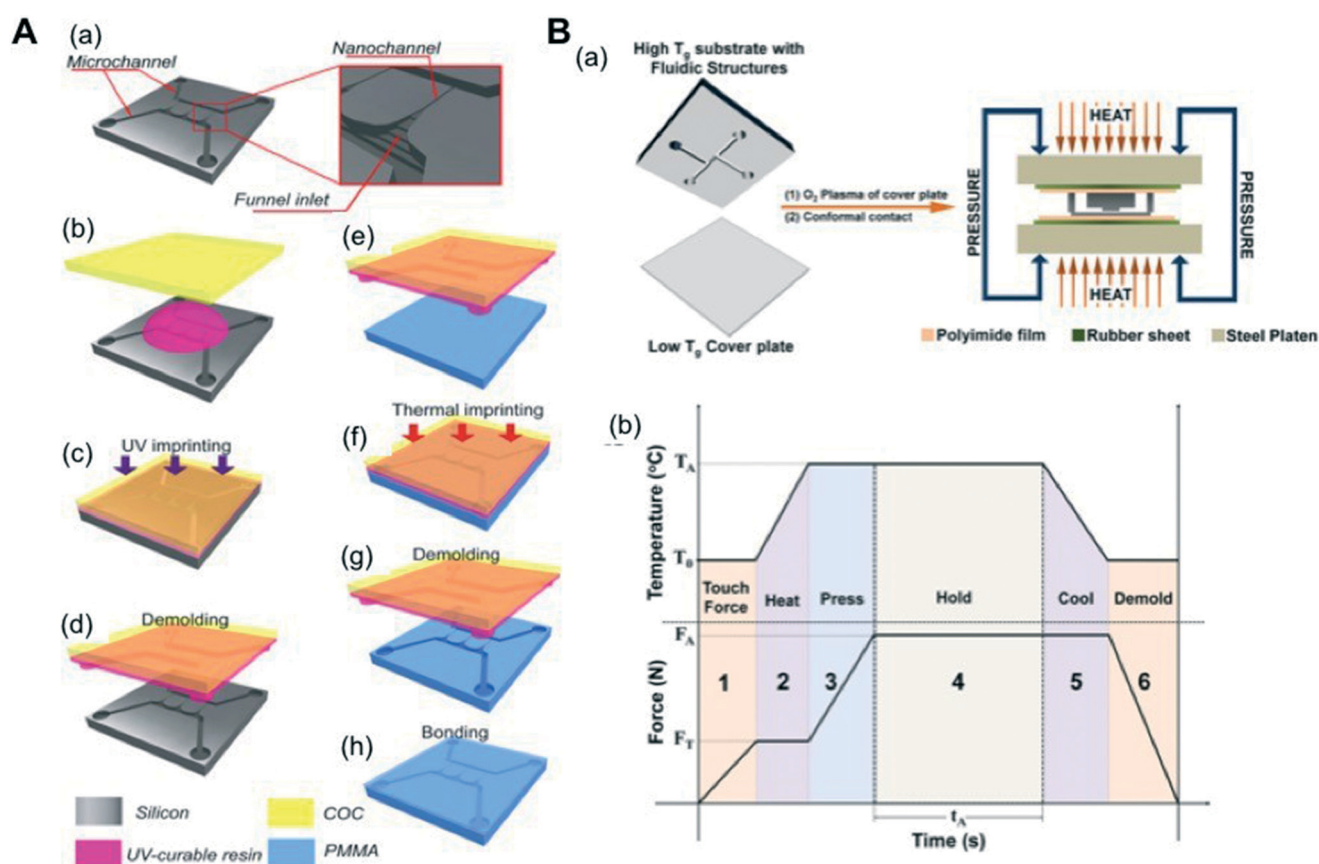
Fig. 2 (A) A schematic of the design and fabrication process of a thermoplastic-based nanofluidic device. (a) Silicon master, which consisted of micron-scale transport channels, nanochannels and a funnel-like inlet for the nanochannels; (b)–(d) fabrication steps to produce a protrusive polymer stamp in a UV-curable resin by imprinting from the silicon master; (e)–(g) fabrication steps to generate nanofluidic structures in PMMA by imprinting from the UV-curable resin stamp; (h) bonding step with a PMMA cover plate to build the enclosed mixed-scale polymer device with microchannels and nanochannels. (B) (a) Schematic of the protocol used for assembly of a hybrid fluidic device and the thermal press instrument. (b) Temperature–pressure process profile showing the six stages for the thermal fusion bonding cycle. See main text for a description of the 6 stages of bonding. Reproduced from Wu *et al.*, *Lab Chip*, 2011, **11**, 2984–2989 and Uba *et al.*, *Lab Chip*, 2015, **15**, 1038–1049 (with permission from The Royal Society of Chemistry).

Table 1 Various substrate materials, bonding methods and applications of thermoplastic nanofluidic devices

Thermoplastic	Dimension (nm)	Bonding method	Application	Ref.
PMMA	300 × 500, 300 × 140, 72 × 120	NIL	DNA stretching	Guo (2004)
PMMA	200 × 2000	Thermal	NA	Shao *et al.* (2006)
PMMA	10 000 × 80	Thermal	NA	Abgrall *et al.* (2007)
PC	100–900 wide, 200	PDMS seal	NA	Zhang *et al.* (2008)
PMMA, COC, PC	3000/7000 × 100	O$_2$ plasma assisted thermal bonding	DNA transport dynamics and mobilities	Chantiwas *et al.* (2010)
PMMA	240 × 1100	Solvent assisted	DNA stretching	Cho *et al.* (2010)
PMMA	71 × 77	O2 plasma assisted thermal bonding	DNA stretching	Wu *et al.* (2011)
PC	110 × 2000	PDMS seal	Enzyme kinetics	Wang *et al.* (2013)
PMMA	400 × 400	UV/O$_3$ assisted thermal bonding	Biosensor	Liu *et al.* (2015)
PMMA, PET	89 × 84	O2 plasma assisted thermal bonding	NA	Cheng *et al.* (2015)

addition of a solvent leads to solvation of the thermoplastic surface resulting in mobile polymer chains that can diffuse across the solvated layer leading to entanglement of chains.[98] The Hildebrandt parameter provides a measure of the cohesive molecular forces providing key guidance in the selection of a solvent for device bonding. One must ensure that immersion of the substrate into the solvent does not lead to excessive solvent uptake, which may lead to channel deformation.[98]

The surface energy of thermoplastics makes certain direct bonding approaches difficult. Often activation of the surface is used to alter the surface energy allowing for a stronger bond. This can be done with various approaches, such as O$_2$ plasma or UV/O$_3$ treatment.[99–101] Although this treatment may allow for improved surface energy for bonding, it may also impart surface roughness on the substrate and cover plate. When working on the microscale, this surface roughness may be inconsequential. However, surface roughness may introduce unique flow dynamics at the nanoscale. Although some reports have investigated this effect, more research must be done to show the effects of increased surface roughness on nanoscale fluid dynamics.[85,102]

Thermoplastics possess T_g's that are significantly smaller than glass allowing for the fabrication of nanostructures using high production rate modalities such as NIL. However, low T_g's can be detrimental for thermal fusion bonding of devices during assembly. Thermal fusion bonding a cover plate to the substrate possessing the fluidic network involves heating the cover plate and substrate to a temperature near the T_g of the material.[103] Thermal fusion bonding is achieved by either heating the substrate and cover plate to a temperature slightly above their T_g under a constant pressure and time or bonding at a temperature lower than the T_g of the material following UV/O$_3$ or O$_2$ plasma treatment prior to assembly.[47,51,97,101,104] The former approach has been known to result in significant nanochannel deformation while the latter results in devices with weaker bond strength. On the other hand, solvent-assisted bonding can result in dimensional instability due to material embrittlement or dissolution.[103] Unfortunately, these assembly issues can generate low process yield rates, typically <40% (process yield rate = percentage of devices that possess dimensions comparable to design parameters).

In a recent report (see Fig. 2B), thermoplastic nanofluidic devices were developed at process yield rates >90% using a robust assembly scheme in which a high T_g thermoplastic substrate was thermally fusion bonded to a cover plate with a T_g lower than that of the substrate.[85] Device assembly was achieved by bonding an O$_2$ plasma treated cover plate to an untreated substrate at a temperature ~5 °C lower than the T_g of the cover plate. COC (T_g = 75 °C) was used as the cover plate for a PMMA (T_g = 105 °C) substrate due to its excellent optical transmissivity, low autofluorescence,[105,106] low moisture uptake (<0.01%), high temperature tolerance, and chemical resistance. Examples of nanofluidic devices made from thermoplastics and assembled using this method are shown in Fig. 3.

Relevant electrokinetic parameters for nanoscale electrical transport

Electrokinetic transport of molecules in nanochannels is influenced by several physical parameters that include the EDL, zeta potential, surface charge density and the uniformity of those charges, and the electroosmotic flow (EOF). These parameters will be discussed in the context of EK transport in nanochannels in this section. A summary of EK parameters for PMMA nanochannels can be found in Table 2.

An important factor determining transport processes is the Debye length, λ_D. For a channel filled with a symmetrical 1:1 electrolyte, such as KCl, with ionic concentration c, λ_D can be represented as;

$$\lambda_D = \left(\frac{\epsilon_0 \epsilon_f RT}{2F^2 c}\right)^{1/2} \qquad (1)$$

where R is the gas constant (J mol^{-1} K^{-1}), $\in_0$ is the permittivity of vacuum (F m^{-1}), $\in_r$ is the dielectric constant of the medium, F is the Faraday constant (C m^{-1}), and T is temperature (K). λ_D can range between 1 and 100 nm for electrolyte concentrations between 10 and 0.01 mM.[59]

The ratio of κa, where κ is $1/\lambda_D$ and a is the channel radius, has been used to describe the state of electroneutrality of the bulk solution within a nanochannel/nanoslit.[4,63] When
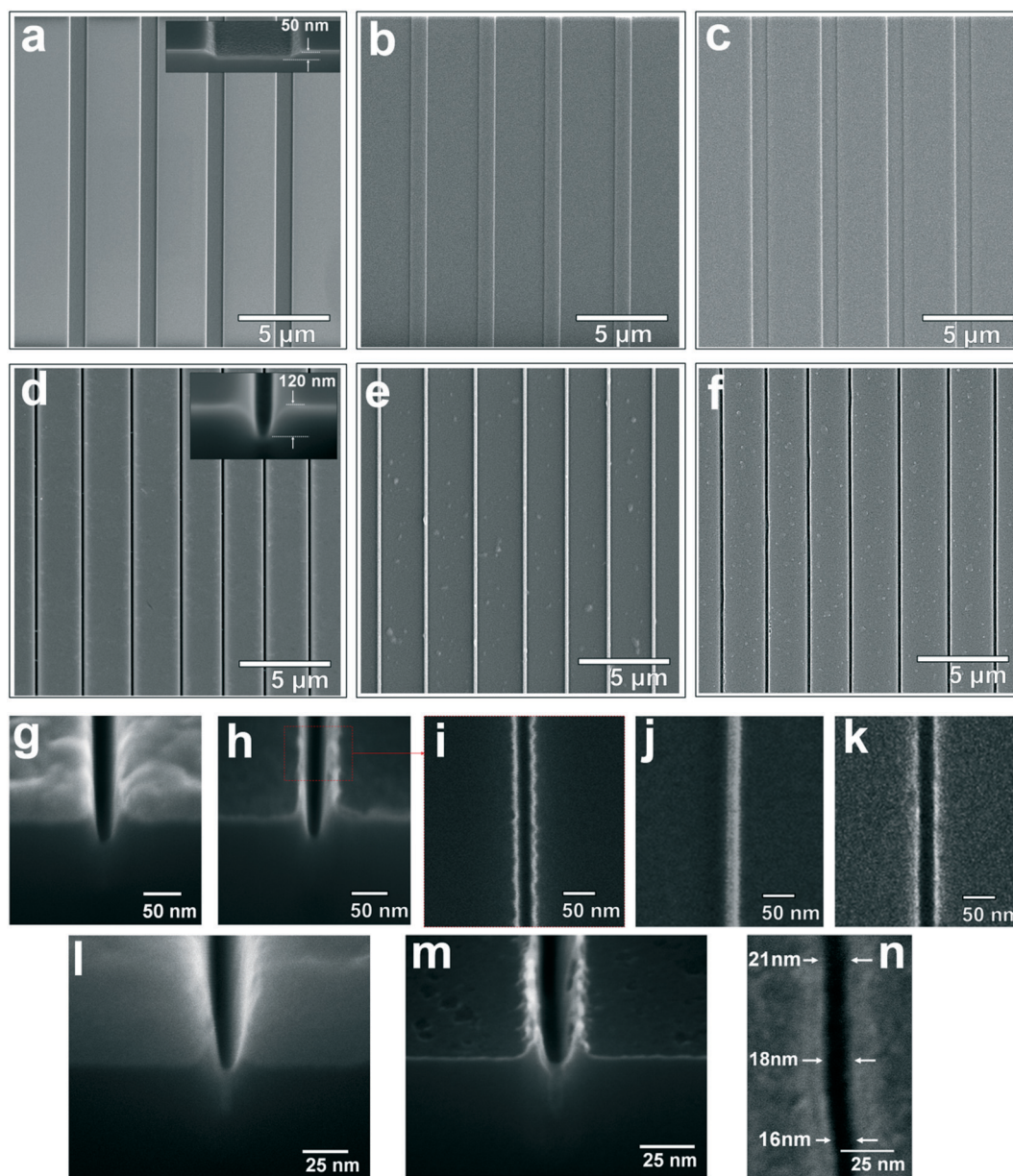
Fig. 3 SEMs of Si masters (a, d, g, h, i, l and m), resin stamps (b, e and j) and nanofluidic devices imprinted in PMMA (c, f, k and n). The device in a–c is a nanoslit device with a width of 1 μm and depth of 50 nm. In d–f, a device with a 120 nm × 120 nm channel is shown. In g–k, a nanofluidic device with 40 × 40 nm channel is shown with a 40 nm thick Al layer that was deposited onto the Si master prior to focused ion beam milling, which was used to generate the nano-structures. In l–n is shown a nanofluidic device with an approximate 20 × 20 nm channel with a 80 nm thick Al layer deposited onto the Si master prior to focused ion beam milling. In all cases, the substrate used was PMMA (glass transition temperature = 105 °C). Figures a–f and m–n were reproduced with permission of The Royal Society of Chemistry from Uba *et al.*, *Analyst*, 2014, **139**. Figures g–k and l are unpublished.

Table 2 Measured and expected EOF values as well as surface charge and zeta potentials for plasma-activated and amine terminated devices investigated at pH 7.8 Reproduced from Uba *et al.*, *Analyst*, (2014) with permission of The Royal Society of Chemistry

Device	Terminating groups	σ_s (mC m^{-2})	ζ (mV)	μ_{eof} (cm^2 V^{-1} s^{-1}) Expected[a]	Measured
Nanoslit	O$_2$-PMMA	−38.3	−57.1	4.53	0.93 ± 0.025
	NH$_2$-PMMA	28.4	45.8	−3.63	−0.82 ± 0.012
Nanochannel	O$_2$-PMMA	−40.5	−59.8	4.74	1.02 ± 0.017
	NH$_2$-PMMA	22.9	38.3	−3.04	−0.75 ± 0.021

[a] Calculated from eqn (6) found in Uba *et al.*, *Analyst* (2014)[70] using the values for σ_s and ζ.

$\kappa a \gg 1$, the solution towards the center of the channel is electrically neutral with a neutral electric potential and displays the classically observed plug-like flow. However, for $\kappa a \approx 1$, there is overlap of the EDL leading to an excess of counterions in the channel and loss of electroneutrality. In this case, the flow profile adopts a parabolic shape and is regarded as Poiseuille-like flow.

Surface charge effects play an integral role in transport processes on the nanometer scale. Electrical conductance measurements across nanochannels filled with ionic salt solutions has been used to evaluate the surface charge density, σ_s. When an external electric field is applied across a nanochannel filled with an ionic salt solution, the measured total electrical conductance (G_T) has been represented as;

$$G_T = 10^3 \left(\mu_{K^+} + \mu_{Cl^-} \right) c N_A \mathrm{e} \cdot \frac{nwh}{L} + 2\mu_{opp}\sigma_s n \frac{(w+h)}{L} \qquad (2)$$

where w, L and h are the nanochannel width, length and height, respectively, N_A is Avogadro's number, c is the electrolyte concentration in mol L^{-1}, n is the number of nanochannels in the device and μ_{K^+} and μ_{Cl^-} are the ion mobilities (for KCl solutions, K$^+$ and Cl$^-$ ions; $\mu_{K^+} = 7.619 \times 10^{-8}$ m^2 V^{-1} s^{-1} and $\mu_{Cl^-} = 7.912 \times 10^{-8}$ m^2 V^{-1} s^{-1}). At high salt concentrations, G_T is dominated by ions in the bulk solution and the measured electrical conductance depends primarily on the nanochannel dimensions and electrolyte concentration.[7,107,108] However, at low salt concentrations, the nanochannels become predominantly filled with counterions and σ_s governs the total ion conductance in the nanochannel.

As reported by Uba et al.,[70] the measured $|\sigma_s|$ of O$_2$-modified PMMA nanoslits (1 μm × 50 nm; width × depth) was ~38.2 mC m^{-2}. This value was less than 60 mC m^{-2} reported by Stein et al.[109] and 214 mC m^{-2} reported by Schoch et al.[107] for glass-based nanoslits measured at pH 8. However, surface charge measurements performed in a nanoslit hybrid device – PMMA substrate bonded to oxygen plasma treated COC cover plate −$|\sigma_s|$ was 57.3 mC m^{-2}.[85] The difference in surface charge density was attributed to more carboxyl groups generated on COC compared to PMMA when treated under similar oxygen plasma conditions.[110,111] UV/O$_3$ activation of the device post-assembly was reported to result in a 4.5% higher surface charge due to the increase in the density of surface carboxylates upon UV/O$_3$ activation of the PMMA substrate. The measured $|\sigma_s|$ in PMMA NH$_2$-modified nanoslits was 28.4 mC m^{-2}. In the case of 120 nm × 120 nm nanochannels, the surface charge densities were 40.5 mC m^{-2} and 22.9 mC m^{-2} for the O$_2$- and NH$_2$-PMMA devices, respectively.

EOF is present in nanochannels carrying a surface charge as is the case for microchannels. Several articles have reported the EOF of nanochannels measured using the current monitoring method.[112] Uba et al.[70] recently showed that the EOF of O$_2$- and NH$_2$-modified PMMA nanochannels were $1.02 \pm 0.02 \times 10^{-4}$ cm^2 V^{-1} s^{-1} and $-0.75 \pm 0.02 \times 10^{-4}$ cm^2 V^{-1} s^{-1}, respectively, as seen in Table 2. The values reported for the O$_2$-PMMA nanochannels were shown to be similar to that

reported by Menard et al.[28] for fused silica nanochannels (≤100 nm in width and depth) measured using 2× TBE with 2% polyvinylpyrrolidone acting as an EOF suppressor (0.79 ± 0.01 × 10^{-4} cm^2 V^{-1} s^{-1}) and ~36 ± 4% lower when compared to fused silica channels measured with 2× TBE (1.58 ± 0.01 × 10^{-4} cm^2 V^{-1} s^{-1}).

Nanochannels for the analysis of biopolymers

Nanofluidic channels have been used for the analysis of biopolymers with DNA being the most reported. Most applications for DNA analysis involves DNA linearization by confinement induced by the nanofluidic device. DNA linearization has been achieved using a variety of nano-systems including nanoslits,[101] nanochannels,[113] and circular or diamond shaped nanopillars.[20,81,114] Unlike other linearization techniques, which exerts a high stretching force at an anchored end that decreases along the length of the molecule, nano-confinement allows the entire confined DNA molecule to be exposed to the same confinement force.[77]

DNA confinement in nanochannels

The physical geometry of DNA molecules can be described by three parameters; the contour length, L_c, persistence length, l_p, and the effective width, w_{eff}.[115] L_c refers to the total length of DNA when it is fully stretched while l_p describes the local rigidity of DNA imposed by its double helical structure. On length scales smaller than l_p, a DNA molecule is considered rigid, while it is flexible at length scales larger than l_p. The l_p and w_{eff} of dsDNA in 0.1 M aqueous NaCl are ~50 nm (150 bp) and 2 nm, respectively.[116]

In solution, a negatively charged polymer like DNA will occupy a finite volume of space, with an excluded volume around itself preventing other molecules to enter this excluded volume due to steric hindrance, repulsive effects and interactions with the solvent. This self-avoidance was introduced by Flory[117,118] and later generalized to the semi-flexible case by Schaefer et al.[119] According to Flory–Pincus, a biopolymer in solution is characterized by the radius of gyration,

$$R_G \cong \frac{R_F}{\sqrt{6}} \qquad (3)$$

where R_F, which is the end-to-end length, is represented as ($l_p \times w_{eff}$)$^{1/5}$ $L_c^{3/5}$. Based on eqn (3), R_G would be ~560 nm and 1140 nm for λ (48.5 kbp) and T4 (169 kbp) DNA, respectively.

Previous reports have shown that a DNA molecule confined in a nanochannel will stretch along the channel axis to a substantial fraction of its L_c.[120] Confinement elongation of genomic-length DNA has several advantages over alternative techniques for extending DNA, such as flow stretching or stretching based on tethering. Confinement elongation does not require the presence of a known external force because a molecule in a nanochannel will remain stretched in its

equilibrium configuration allowing for continuous measurements of length.[80]

In confined spaces, where R_G is much larger than the geometrical average depth, D_{av}, of the nanochannel, the number of available configurations of the polymer is reduced. Two main confinement regimes exist that depend on differences between D_{av} and l_p. When $D_{av} \gg l_p$, the molecule is free to coil within the nanochannel and stretching is entirely due to excluded volume interactions between different coiled segments of the polymer separated along the backbone. Coiling of the molecule can be broken into a series of blobs with diameter L_b, while the stretching is a result of repulsion between the blobs; this is known as the deGennes regime.[121] Within the blobs, the confinement force is only a weak perturbation while each blob retains the property of the bulk polymer. The extension length of the molecule, R_x, can be calculated using;

$$R_x = L_c \left(\frac{w_{eff} l_p}{D_{av}^2} \right)^{1/3} \tag{4}$$

where $D_{av} = \sqrt{D \times h}$ and is the geometrical average of the two confining dimensions.

As the channel width decreases and $D_{av} \ll l_p$, the stretching is no longer a result of volume exclusion but an interplay between confinement and the intrinsic elasticity of the DNA molecule. The strong confinement prevents the molecule from forming loops within the nanochannel. Back folding becomes energetically unfavorable and stretching becomes a result of deflection of the molecules with the channel walls. The average length between these deflections is of the order of the Odijk length scale; $\lambda_p \cong (D_{av}^2 l_p)^{1/3}$. This regime is referred to as the Odijk regime.[122,123] For a small average deflection, θ, R_x is represented as;

$$R_x = L_{cont} \cos \theta \cong L_{cont} \left[1 - 0.361 \left(\frac{D_{av}}{l_p} \right)^{2/3} \right] \tag{5}$$

Recent reports have revealed the existence of an intermediate region between the deGennes and Odijk regimes – extended deGennes regime – where the excluded volume interaction is weaker than the thermal energy.[124,125]

Effect of ionic environment of DNA stretching

According to Reisner et al.,[120] variations in the ionic strength affect the configuration of a DNA molecule by modulating the range of electrostatic interactions between the charges on the phosphate backbone. Electrostatic interactions in electrolyte solutions are screened over a characteristic scale known as the Debye length. The geometry of DNA results in two types of electrostatic interactions:[80] (i) interactions between charges separated in contours that create repulsion between

back looping segments resulting in an effective DNA width (w_{eff}) that is larger than the intrinsic width w_0; and (ii) local repulsive interactions between charges separated by less than the Debye length in contour resulting in an increase in l_p. The mechanisms of these interactions determine the ionic strength variation of the extension over an ionic strength range.

Applications of thermoplastic nanochannels

DNA analysis in polymer nanofluidic devices

In 2004, Guo and coworkers studied the stretching of DNA in size-controllable PDMS-PMMA devices at 3 different nanochannel dimensions. T5 phage DNA was stretched in densely packed nanochannel arrays with dimensions of 300 nm × 700 nm, 300 nm × 500 nm and 75 nm × 120 nm. They observed stretching of 15%, 30% and 95%, respectively, in these devices showing channel size dependence on stretching as predicted by de Gennes and Odijk.[126]

PMMA and COC nanofluidic devices have been used for DNA elongation as well. Thamdrup et al.[127] measured the extension of DNA compared to theoretical models using T4 DNA (169 kbp; 54 nm in length). According to their theoretical calculations, dye-labeled T4 DNA (1 dye : 5 bp) has $L_c = 70$ nm and $l_p = 62$ nm. For their experiments, DNA was electrophoretically driven one at a time into PMMA nanochannels (250 nm × 250 nm). DNA extension (L_{ext}) was recorded for 10 different molecules (Fig. 4A). The L_{av} of λ-DNA was found to be 13.5 ± 0.5 μm, which agreed well with the calculated extension length (13.6 μm; 24% of the dye labeled length of T4) predicted from the deGennes model. The uncertainty of the average extension length was given by u_{av}; $u_{av} = \sigma_{av}/\sqrt{N}$, where N is the number of frames analyzed. As they suggested, average DNA extension deviation (σ_{av}) was strongly dependent on small thermal fluctuations around L_{av} that could be suppressed by analyzing multiple frames. Other factors such as variation of cross-sectional dimensions of the polymer nanochannels, variation of the degree of interaction and the existence of several different lengths of DNA molecules may have also contributed to the variation of L_{av}.

In 2011, Utko et al.[49] was able to produce different nanoscale arrays of channels by injection molding onto a thick COC disk. Three different arrays of nanochannels were produced, each with an array consisting of 80 nanochannels; 400 nm wide straight channels, 240 nm wide straight channels and tapered nanochannels with decreasing width from 1040 nm to 140 nm; in all cases the depth was 150 nm (Fig. 4B). Nanochannels were sealed with a 150 μm thick COC plate using thermal fusion bonding. For the extension experiments, λ-DNA in 0.5× TBE buffer was used and the DNA were electrophoretically moved into the channel and the field was turned off to leave the molecule stationary within the nanochannel. The DNA molecule was fit to a Gaussian pointspread function to extract its position and extension, which
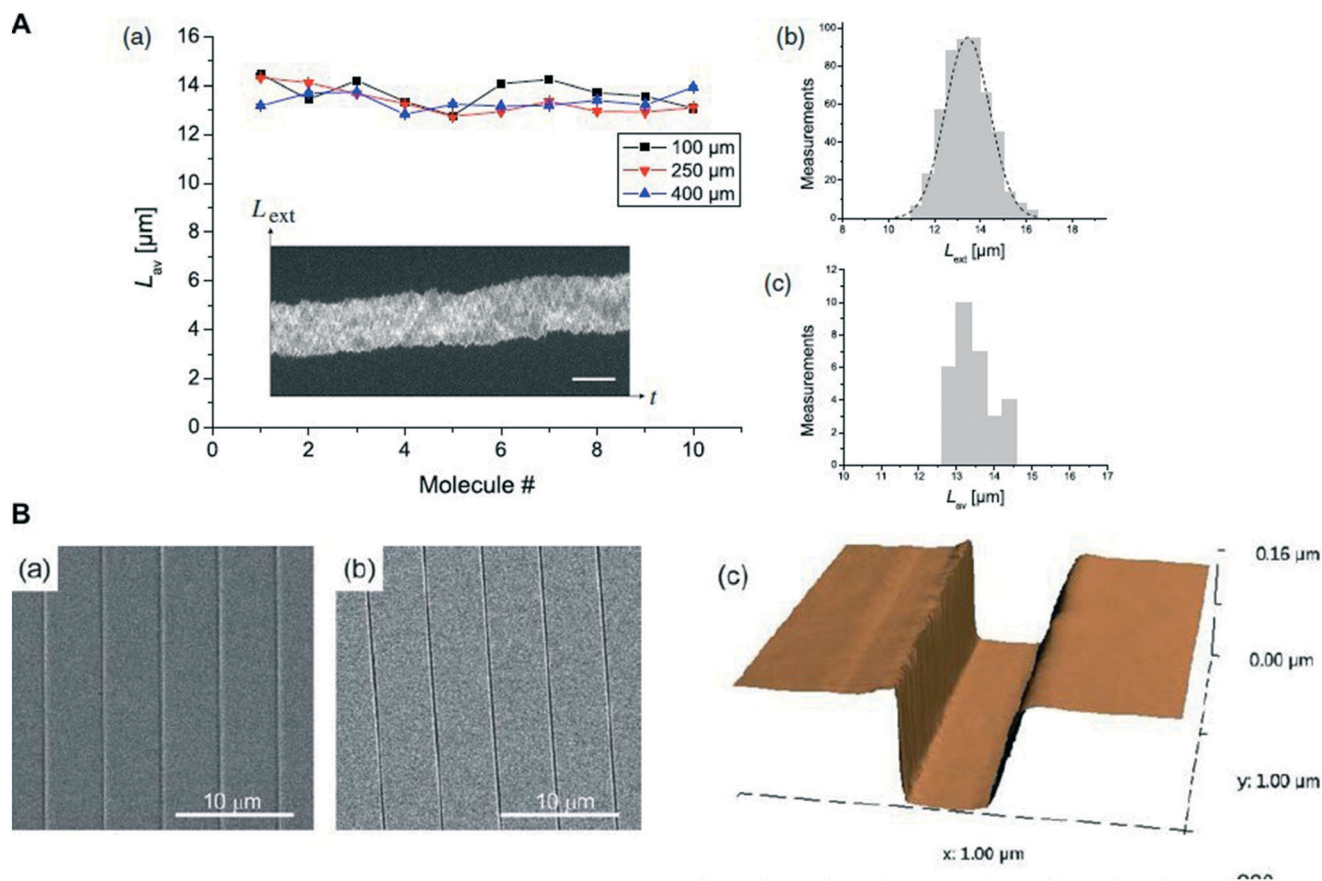
Fig. 4 (A) (a) Graphs showing the average extension length (L_{av}) of 10 different T4 DNA molecules. L_{av} has been measured 100, 250 and 400 μm from the nanochannel entrance for each molecule. The inset shows a typical intensity time-trace of a T4 molecule confined inside a PMMA nano-channel. The scale bar is 10 μm and the time span is 50 s. (b) Histogram of the measured extension lengths (L_{ext}) of DNA molecule 2 positioned 100 μm from the nanochannel entrance. The average extension length, based on an analysis of 500 consecutive frames, L_{av} = 13.4 μm and the standard deviation σ_{av} = 1.0 μm. The dashed line shows the Gaussian curve fit. (c) Histogram of the measured average extension lengths of L_{av} presented in (a). The overall average L_{av} was 13.5 μm with a standard deviation of 0.5 μm. Reprinted from Thamdrup *et al.*, *Nanotechnology*, 2008, **19**, 125301 with permission from IOP Publishing. (B) (a) SEM micrograph of a nickel plate with an array of 240 nm wide and 150 nm high protru-sions. (b) Corresponding nanochannel array injection molded in Topas 5013. To avoid charging effects during SEM imaging, the chip surface was sputtered with 5 nm of gold. (c) Three dimensional AFM image of a channel segment, taken for the same array as in (b). Adapted from Utko *et al.*, *Lab Chip*, 2011, **11**, 303–308 with permission of The Royal Society of Chemistry.

was then mapped to a specific location in the nanochannel. They also studied the autofluorescence intensity of COC by bleaching nanochannel areas by exposing it to a 200 W ha-lide lamp for 20 min and did not find significant bleaching. Their DNA stretching results suggested that the difference in the DNA extension was not only due to thermal fluctuations along the nanochannel, but also associated with the imper-fection of the nanochannel profiles. The average extension of DNA (*r*) was increased with decreasing channel heights according to the results obtained from the tapered nano-channels. They measured the extension of DNA and calcu-lated the power law dependence according to $r \propto D_{av}^{-\alpha}$. They found α = 0.76 ± 0.05, which agreed very well with the results collected using fused silica devices (α = 0.85 ± 0.01), thus confirming COC as an ideal substrate for DNA elongation experiments.

Soper and co-workers explored DNA stretching in thermo-plastic nanofluidic devices using both PMMA and COC sub-strates. Chantiwas *et al.*[51] and Wu *et al.*[97] illustrated the use

of thermoplastic nanoslits (COC) and nanochannels (PMMA) for DNA stretching. Chantiwas *et al.*[51] reported that the low EOF in COC devices negated the need for an EOF suppressor compared to glass-based devices. At 25 V cm^{-1}, translocation velocities of λ-DNA were found to be 8.2 ± 0.7 × 10^{-4} cm^2 V^{-1} s^{-1} for PMMA and for COC devices, it was 7.6 ± 0.6 × 10^{-4} cm^2 V^{-1} s^{-1} in 7 μm wide and 100 nm deep nanoslits. DNA extension lengths were measured to be 46% for PMMA and 53% for COC nanoslit devices compared to the full contour length of a dye-labeled λ-DNA molecule. Wu *et al.*[97] observed increased elongation of DNA in 100 nm × 100 nm (~50%) and 75 nm × 75 nm (~81%) nanochannels compared to PMMA nanoslits as would be expected because of the smaller size of the nanochannels compared to nanoslits.

Uba *et al.*[70] recently discussed λ-DNA stretching in surface modified thermoplastic nanoslits. Stretching of DNA was mea-sured in the absence of an electric field. According to the deGennes theory, stretching of ~25% for λ-DNA would be pre-dicted in a 100 nm × 100 nm nanochannel. They observed an

elongation length of 6.88 μm (34%), which was higher than that predicted according to the deGennes theory. The authors suggested that the increased stretching was due to interfacial surface forces arising from the charged nanochannel walls. One interesting discovery in this study was the presence of "stick-slip" motion at low electric fields and low buffer concentrations. In 0.5× (44.5 mM) TBE, they observed "stick-slip" motion with field strengths <150 V cm^{-1} suggesting the possibility for dielectrophoretic trapping. When a charged molecule is in intermittent motion inside a nanochannel with a thick EDL, the interfacial forces could likely be higher than the driving force, resulting in "stick-slip" motion. At higher buffer concentrations (2× TBE, 180 mM), DNA velocity had a linear increase with electric field strength suggesting the absence of dielectrophoretic trapping.

Genomic mapping within thermoplastic nanochannels

One application of DNA stretching within nanochannels is genomic mapping.[128–130] For mapping, molecular markers are used to label sequence specific sites within the genomic DNA.

To facilitate mapping of specific sites within genomic DNA, it is important to stretch the DNA to near its full contour length. Currently, commercial devices such as that marketed by BioNanoGenomics fabricate devices in inorganic substrates using deep UV lithography have been used for this application.[130,131] Das et al.[132] used a Si device bonded with glass to identify specific sequence variations in stretched DNA. They investigated linearized 115 kbp circular DNA BAC clones of MCF7-3F5 cells in 60 nm × 100 nm nanochannels by achieving ~65% DNA stretching with respect to its full contour length. Even though optical genomic mapping has been reported on Si-based devices, it is yet to be reported in thermoplastics.

Soper and coworkers reported efforts to stretch DNA by reducing the channel dimensions in thermoplastics. Fig. 5A shows the stretching of T4 DNA in different sizes of plastic nanochannels. In all cases, the signal-to-noise (SNR) ratio was improved using a hybrid device consisting of a COC cover plate and PMMA substrate.[133] Fig. 5B shows DNA extension (ε) changes with D_{av}. Theoretical de Gennes regimes are shown in the red dashed line and Odijk regime was represented as the blue dashed line (see Fig. 5B). When D_{av} was larger than 200 nm, the experimental extension curve fit well with the de Gennes regime and when D_{av} = 35 nm, it fit well to the Odijk regime. However, stretching in nanochannels with dimensions of 190 × 95 nm, 150 × 60 nm and 110 × 25 nm resulted in stretching that did not fit with either regime, rather it fell between the two regimes (Fig. 5A; nc3 to nc5).

Thermoplastic devices for nanoelectrophoresis

As previously discussed, unique phenomena such as EDL overlap and increased surface area to volume arise in the nanodomain. For this reason, efforts have been invested into electrophoretic separations using nanoscale columns. Research has primarily focused on the use of fused-silica nanochannels/nanoslits due to the well characterized surface chemistry that is highly ordered and homogenous; however, fabrication of these devices is costly and time consuming. Thus, investigations of thermoplastic nanochannels for nanoelectrophoresis are developing. Furthermore, investigations to understand the effects of thermoplastic surfaces on nanoscale separations has been performed.

O'Neil et al.[67] utilized super resolution microscopy to explore the heterogeneity of activated COC and PMMA substrates to understand the density and distribution of generated surface confined –COOH groups on thermoplastics.
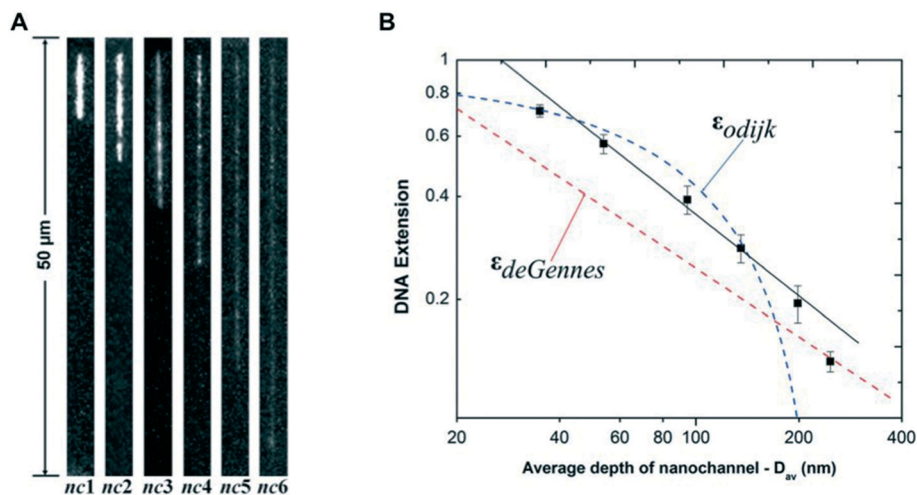

Fig. 5 (A) Unprocessed representative frames of T4 DNA molecules elongated in enclosed hybrid-based nanochannel devices. Images were acquired at 10 ms exposure time with the driving field turned-off. Note that nc6 = 35 × 35 nm. (B) Log–log plot showing T4 DNA extension as a function of the geometric average depth of the nanochannels. The DNA extension was normalized to a total contour length (L_c) of 64 μm for the dye-labeled molecules. The red and blue dashed lines are the deGennes and Odijk predictions, respectively. The black solid line is the best power-law fit to the data points obtained from the nanochannels with an average geometric depth range of 53 nm to 200 nm. Reproduced from Uba et al., Lab Chip, 2015, 15, 1038–1049 with permission from The Royal Society of Chemistry.
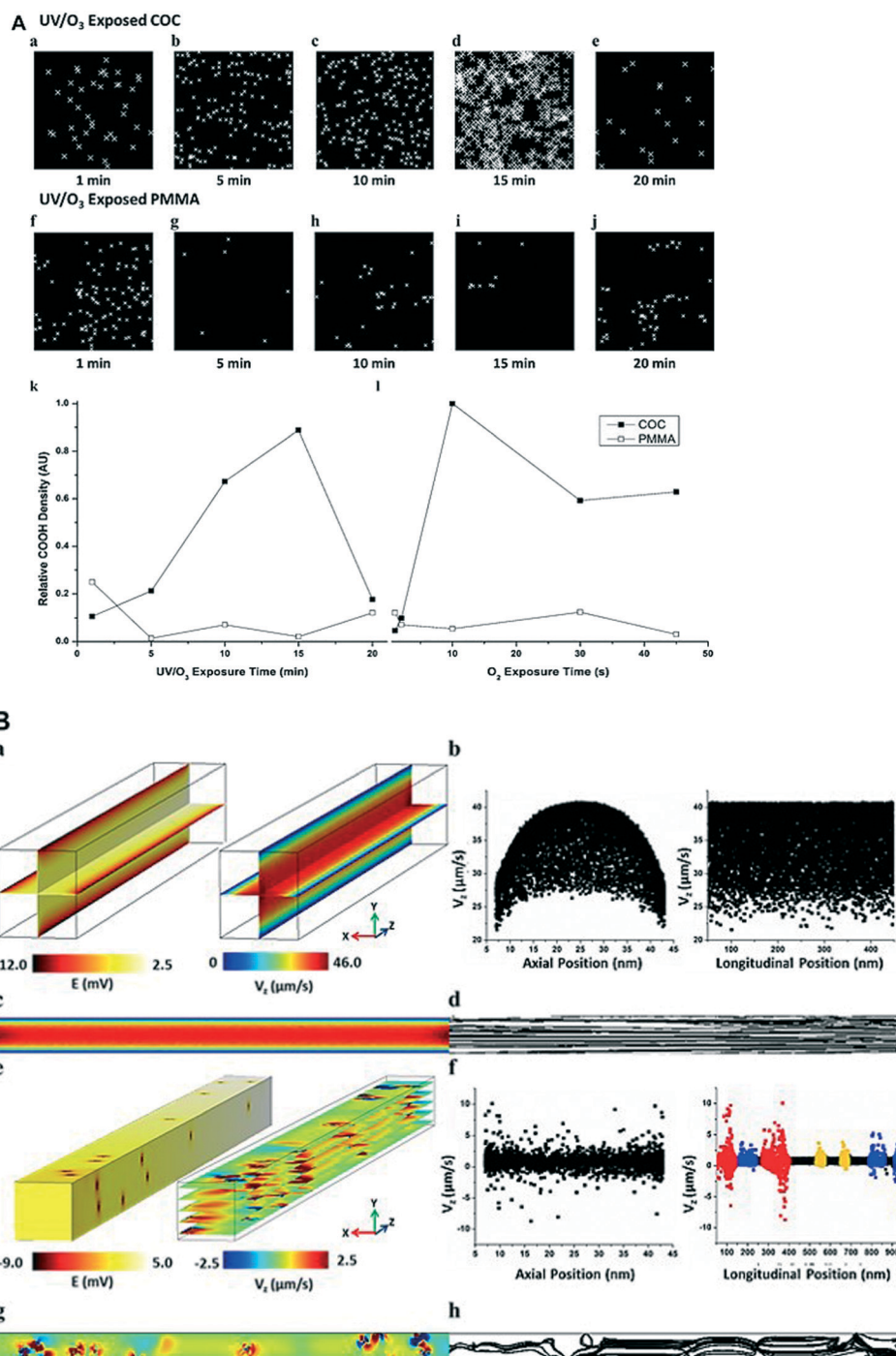
Fig. 6 (A) Representative STORM images of 1 µm² (a–e) COC and (f–j) PMMA exposed to 1, 5, 10, 15, and 20 min UV/O₃ radiation, respectively. Relative –COOH density vs. exposure time for (k) UV/O₃ and (l) O₂ plasma-modified COC (closed squares) and PMMA (open circles). Lines are for visual purposes only. UV/O₃ and O₂ plasma exposure conditions were kept constant. All total localizations were normalized to the greatest localization density, which was for COC exposed to 10 s of O₂ plasma. (B) (a) COMSOL simulation showing the electric potential (left) and velocity magnitude (right) for a channel with uniform surface charge; (b) velocity vs. axial (right) and longitudinal (left) position to show the EOF flow profile for a channel with uniform surface charge; (c) one slice of the velocity magnitude of a uniform channel; (d) streamline of the same velocity slice depicted in (c); (e) COMSOL simulation showing the electric potential (left) and velocity magnitude (right) where single point charges were mapped onto the nanochannel surfaces using the –COOH locations (centroids) obtained by STORM analysis of a COC surface exposed to 5 min UV/O₃ activation. (f) Velocity vs. axial (right) and longitudinal (left) position to show the EOF flow profile for the channel with non-uniform surface charge. The colors in the velocity vs. Z position graph (right) represent an area in the channel with >5 (red), 3–4 (blue), and 1–2 (yellow) –COOH group(s) within 20 nm of each other. (g) One slice of the velocity profile to show fluid flow recirculation. (h) Streamline of the same velocity slice depicted in (e) to emphasize the fluid recirculation at areas with –COOH. Reprinted with permission from O'Neil et al., Anal. Chem., 2016, 88, 3686–3696 (American Chemical Society).

They showed that –COOH groups were heterogeneously distributed over the plastic substrate following activation and both the relative density and distribution were dependent on the activating dose. COC demonstrated a higher surface density of –COOH groups when compared to PMMA (Fig. 6A). COMSOL investigations into the contribution of this heterogeneous distribution of surface charge on the EOF showed distortion; however, the lower surface charge density compared to glass led to an overall lower EOF, thus an expected minimal contribution to electrophoretic zonal dispersion because the solute's electrophoretic mobility would dominate (Fig. 6B). They confirmed this finding by performing nanoscale electrophoresis within COC nanoslits of fluorescently labeled polystyrene (PS) particles. Evidence of stick/slip motion was observed at low field strengths (<200 V cm^{-1}) leading to longer migration times and greater zonal dispersion. At higher field strengths (>300 V cm^{-1}), solutes were seen to transverse the channel with fewer wall interactions leading to a faster migration time and less dispersion.

Weerakoon-Ratnayake et al.[134] investigated the separation of silver nanoparticles (AgNP) within nanoscale PMMA columns. Dark field microscopy was used to track the transport of AgNPs within these devices with varying slit dimensions, buffer ionic strengths and applied electric fields. The authors were able to demonstrate the separation of AgNPs based on size without the addition of buffer additives, which was not possible with microdevices. The best resolution was achieved at high electric field strengths, which was not possible in microscale devices due to Joule heating (Table 3). Low field strengths (<200 V nm^{-1}) caused decreased resolution and plate numbers due to the presence of stick/slip motion of the AgNPs (Fig. 7).

Single-molecule sequencing (SMS) by time-of-flight (ToF) strategies is an immerging field of research. Along these lines, Oliver-Calixte et al.[135] showed the capability of immobilizing λ-exonuclease onto PMMA substrates to clip dsDNA molecules into their constituent mononucleotides (Fig. 8A). Several simulation studies have shown the possibility of the electrophoretic separation of single mononucleotides using thermoplastic-

based nanochannels.[71,72] Novak et al.[71] suggested the possibility of separating deoxynucleotide 5′-monophosphates (dNMPs) within a 5 nm wide channel (Fig. 8B). Their study, based on the adsorption/desorption properties of the dNMPs, suggested that controlling the wettability of the surface may be a reliable way to separate dNMPs using nanocolumns. In a more recent article, Xia et al.[72] showed separation of dNMPS under high electric field strengths and varying roughness of the nanocolumns. They observed a change in the elution order of the dNMPs depending on the roughness of the nanochannels walls.

Other applications of thermoplastic nanochannels

Thermoplastic nanofluidic devices have also been used for the electrochemical detection of small molecules,[136] investigation of enzyme reaction kinetics[137] and identification of single nucleotide polymorphisms (SNP).[138]

Liu et al.[136] developed a protocol for the integration of microelectrodes onto a PMMA nanofluidic device for the electrochemical detection of biotin at concentrations as low as 1 aM. This device was combined with nanoparticle crystals and the use of a PMMA substrate that showed better signal-to-noise and a higher sensitivity with easy fabrication compared to a glass-based device.

Yang et al.[138] fabricated a high density array of nanochannels with carboxyl terminated PMMA for the immobilization of molecular recognition agents, MRAs (Fig. 9A). An oligodeoxynucleotide (ODN-A) labeled with carboxyfluorescein was immobilized onto nanochannel walls and hybridized with rhodamine labeled ODN-B, forming a 14 base pair double stranded DNA with 5 unhybridized bases to be used as the MRA. Target single stranded DNA molecules were passed through the nanochannels and allowed to interact with the double stranded DNA complexes. Displacement of the ODN-B from the nanochannels varied depending on the thermodynamic stability of the newly formed double stranded DNA, which was determined by the presence and location of SNPs on the target DNA. This device was able to detect SNPs as well as discriminate SNPs at various locations. They utilized the nanochannels to detect SNPs in alcohol dehydrogenase 2 (ALDH2), which can be used for the evaluation of organ susceptibility to alcohol damage. The sequence containing one SNP showed a 50% higher displacement of the oligodeoxynucleotide probe, thus allowing for the identification of wild type and SNP DNA.

Wang et al.[137] fabricated a y-shaped nanofluidic chip in PC and sealed the device with PDMS. This y-shaped device was used to allow homogenous mixing of an enzyme and ligand to observe "free state" enzyme reaction kinetics in nano-confinement (Fig. 9B). Glucose oxidase and D-glucose were chosen as the model enzyme–ligand pair. The reaction product, hydrogen peroxide (H_2O_2) was electrochemically detected and it was determined that the "free state" activity increased significantly compared to the immobilized and bulk solution enzyme.

Table 3 Electrophoretic properties of 60 and 100 nm AgNPs at different nanoscale electrophoresis operating conditions Reproduced with permission from Weerakoon Ratnayake et al., Anal. Chem., 2016, **88**, 3569–3577 (American Chemical Society)

Depth of nanoslit	150 nm		150 nm		400 nm	
Citrate buffer Concentration	2.00 nM		0.05 mM		0.05 mM	
Particle size (nm)	60	100	60	100	60	100
Field strength (V cm^{-1})	Plate number (N)					
100	723	694	303	233	422	371
200	987	1320	486	570	737	1090
500	2350	3000	1220	1220	1750	2320
1500	6800	9270	4370	4250	5100	6370
Field strength (V cm^{-1})	Resolution (R)					
100	0.089		0.022		0.58	
200	0.77		0.33		0.26	
500	0.57		0.74		0.51	
1500	0.67		1.1		0.61	
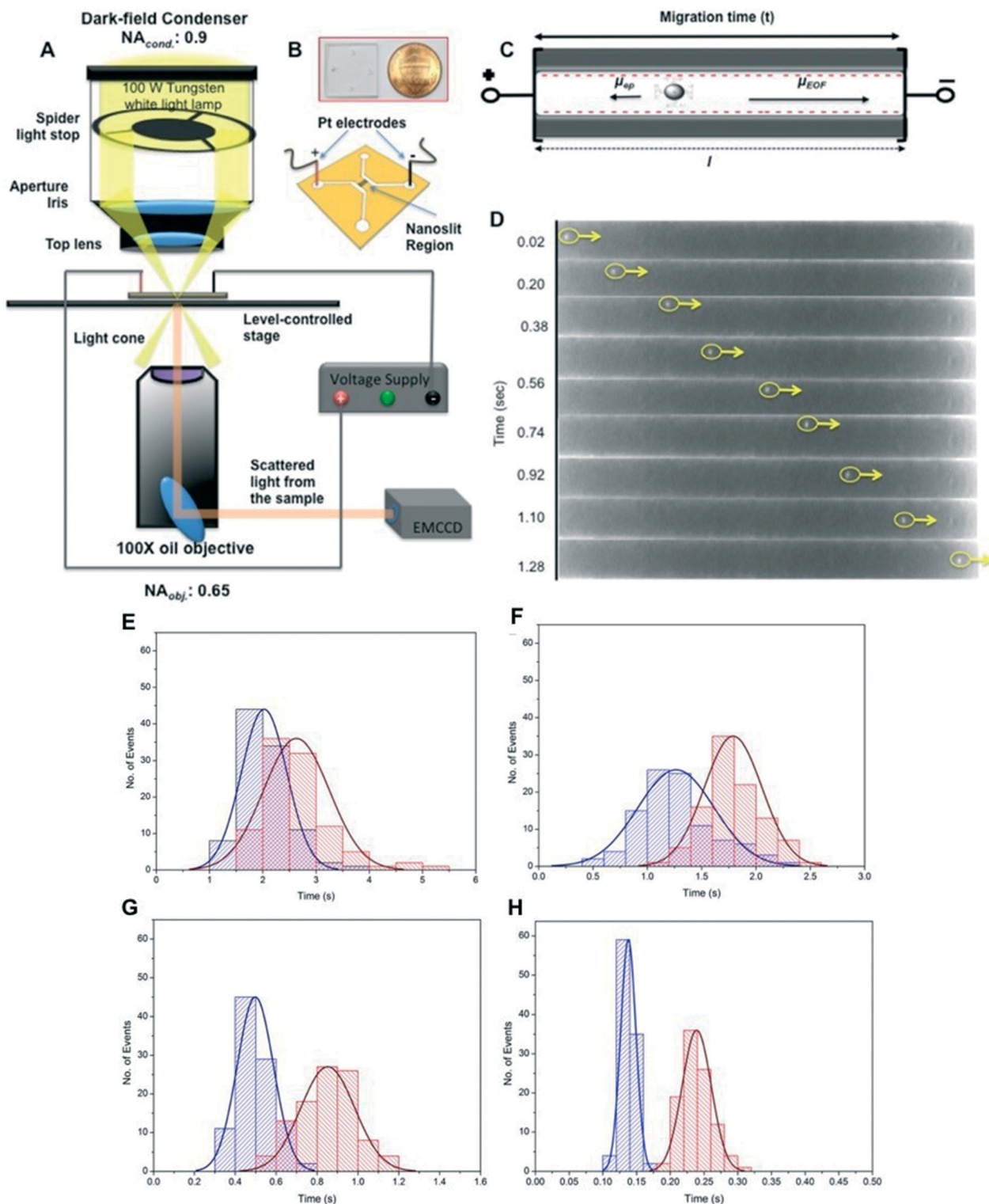
Fig. 7 (A) Schematic of the dark field microscope and the experimental setup. The sample was mounted on a level-controlled microscope stage. While the spider stop controlled white light missed the objective, only scattered light from the sample entered the objective. (B) Image of the PMMA nanofluidic chip and a schematic of the device with nanoslits. (C) Schematic of the nanoslits when an external electric field was applied. Electroosmotic flow was from anode to cathode while the electrophoretic mobility of negatively charged AgNPs was toward the anode. (D) Representation of a translocation event for a 60 nm AgNP in a nanoslit. Time-lapse image sequence of the single AgNP event with an external field strength = 200 V cm^{-1}. The particle translocation direction was from anode to cathode (same direction as EOF) with a translocation time of 1.3 s. Dimensions of the nanoslits were 100 μm in length and 150 nm deep. Histograms of translocation events for 60 nm AgNPs (blue) and 100 nm AgNPs (red) in 150 nm nanoslits with a running buffer of 0.05 mM citrate. Each histogram includes 100 events at a bias voltage of (E) 100 V cm^{-1}, (F) 200 V cm^{-1}, (G) 500 V cm^{-1}, and (H) 1500 V cm^{-1}. Note that the time axes have different scales depending on the electric field. Weerakoon Ratnayake et al., Anal. Chem., 2016, 88, 3569–3577 (American Chemical Society).
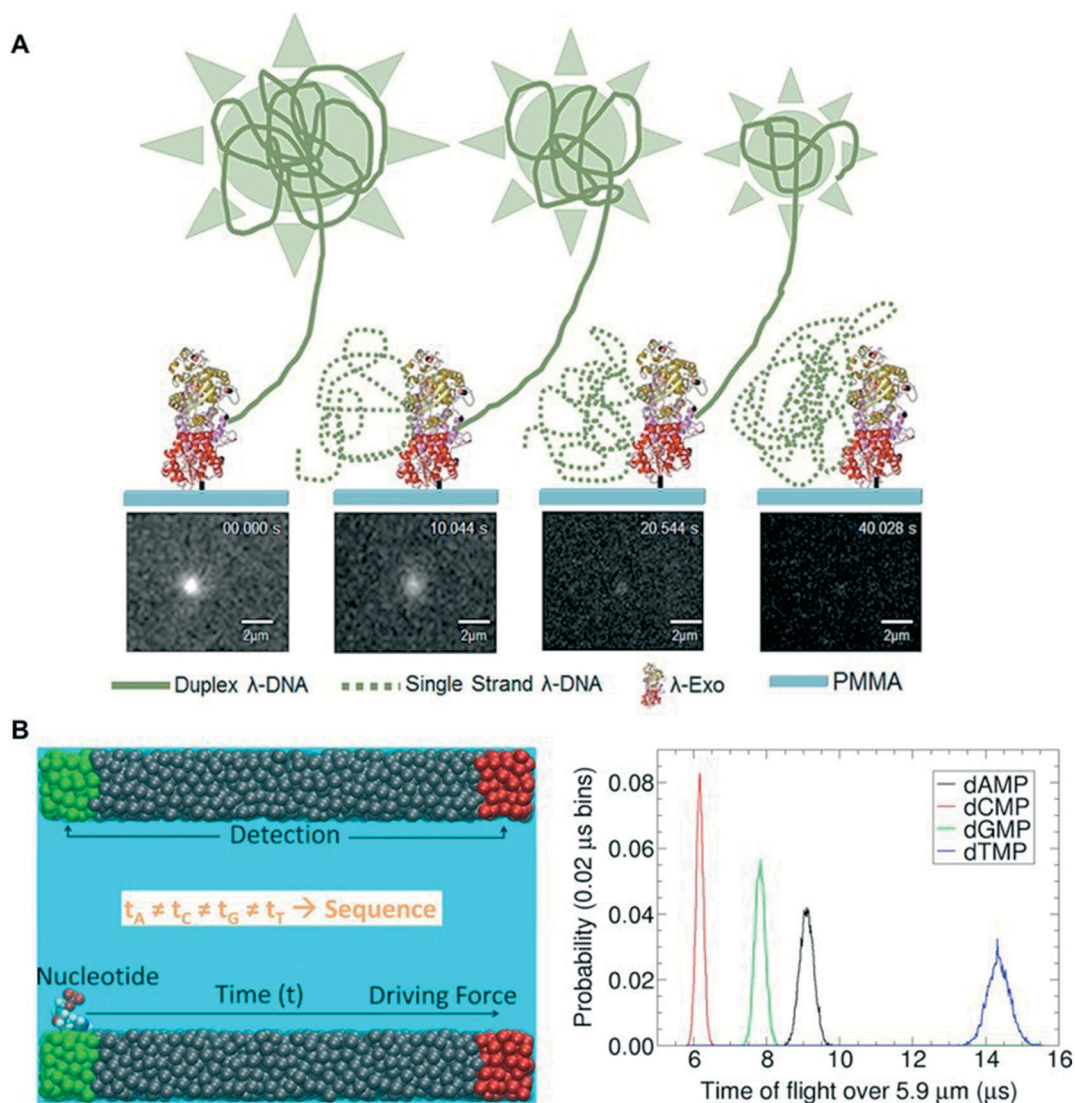
Fig. 8 (A) Representative schematic of λ exonuclease immobilized onto a PMMA pillar as it processively cleaves dNMPs from a double stranded (ds) DNA molecule. Fluorescence images showing the digestion of dsDNA by λ exonuclease immobilized onto a PMMA pillar. Oliver–Calixte *et al.*, *Anal. Chem.*, 2014, **86**, 4447–4454 (*ACS Author's Choice article*, American Chemical Society). (B) Molecular dynamic simulations of the translocation of single dNMP molecules within nanochannels showing the separation of dCMP, dGMP, dAMP and dTMP (Novak *et al.*, *J. Phys. Chem. B*, 2013, **117**, 3271–3279, American Chemical Society).

Commercialization of nanofluidics for biomedical applications

Commercialization of nanofluidic devices using thermoplastic substrates holds great promise for various application areas such as genomic mapping and DNA sequencing, but still faces challenges. For example, it is necessary to understand physical phenomena occurring in nanochannels *via* theory and simulations and supplemented with experimentation that can guide production of optimal nanoscale devices. These areas are still in a developmental stage, especially in attempting to adequately describe transport processes in this transition region that depend on MD simulations (nanoscale) and continuum theory (microscale). Density functional theory (DFT) may be a helpful by exploiting the use of Stokes and Poisson equations.[139,140] Describing electrical flow in these regions is complicated by the amorphous nature of thermo-

plastics giving heterogeneous surface charge densities. Also, assembly/bonding issues must be addressed for thermoplastic devices <50 nm in critical dimensions. Hybrid thermal bonding techniques may prevent most of the structural deformation associated with thermal assembly, but can provide devices with different material surface properties that can affect device performance, for example creating unusual electroosmotic flow profiles due to different surface charge densities on the substrate and cover plate.

In spite of these challenges, thermoplastic nanofluidic devices can generate cost effective production pipelines that would allow for the dissemination of nanofluidic devices into the community *via* commercialization efforts. There are examples of nanofluidic devices that have reached commercialization. For example, BioNanoGenomics produces a commercial device called the Irys system, which consists of an array
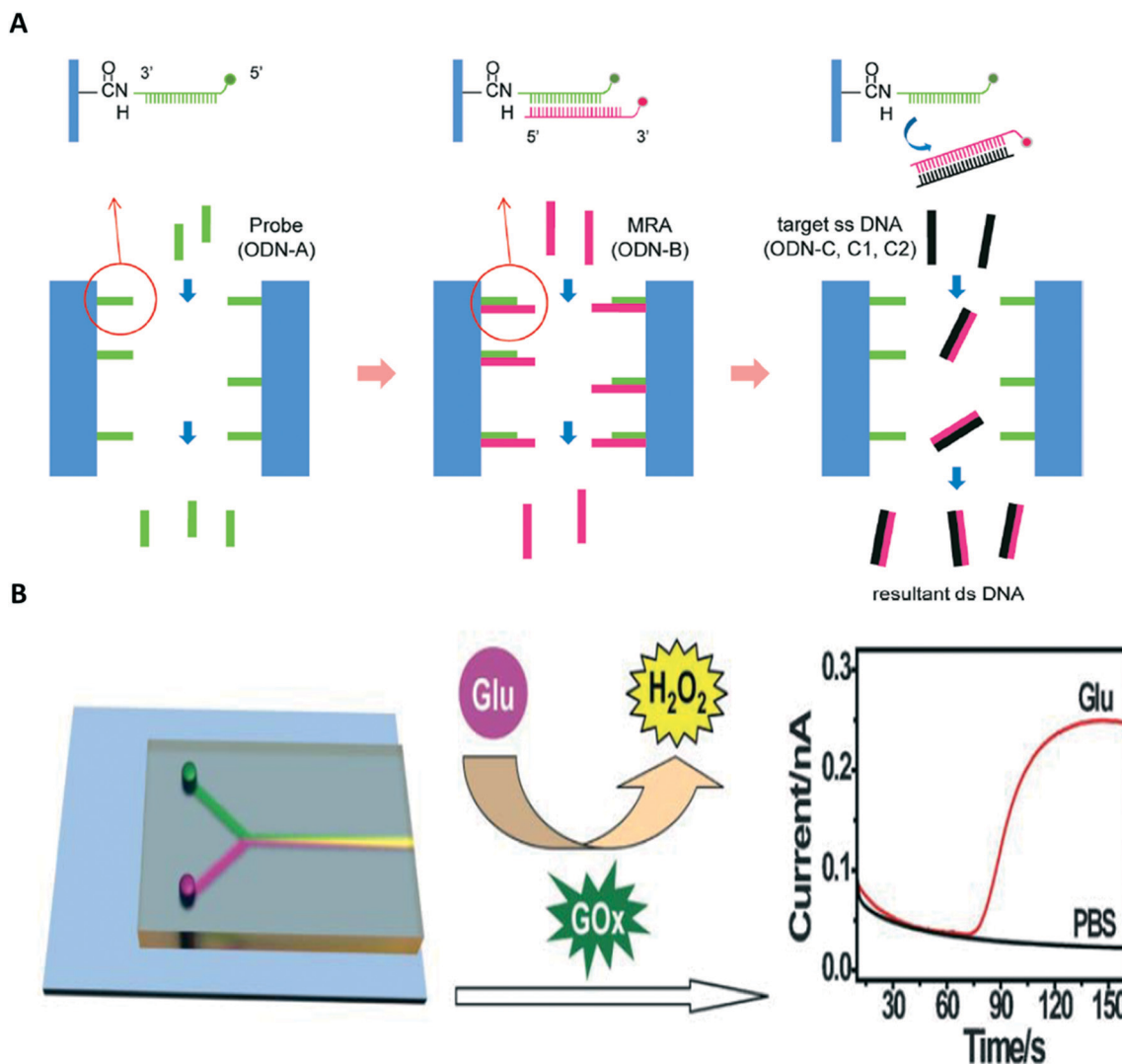
Fig. 9 (A) Schematic illustration for SNP detection based on molecular recognition using DNA-functionalized nanochannels (Yang *et al.*, *Nano Lett.*, 2011, **11**, 1032–1035, American Chemical Society). (B) Schematic layout of a nanofluidics chip. Green and pink colors denote enzyme and substrate, respectively; yellow denotes the reaction product. The product of the enzymatic reaction, hydrogen peroxide, was electrochemically determined as indicated by the rise of the current when the substrate, glucose, was introduced. The working electrode was aligned to the end of the nanochannel with a distance of 20 mm. Reproduced from Wang *et al.*, *Lab Chip*, 2013, **13**, 1546–1553 (The Royal Society of Chemistry).

of nanochannels made in inorganic substrates. The Irys next generation mapping (NGM) chip can handle 1 kb DNAs with an approximate cost of $1000 per chip.[141,142]

Oxford nanopore produces commercial DNA sequencers that utilize label-less detection. They've released pricing information for the MinION Mkl sequencer suggesting $500–$900 per nanofluidic device. These devices consist of arrays of biological nanopores suspended on a thin membrane. The maximum DNA sequencing yield per flow cell was reported to be 0.5–1 gb.[143]

Unfortunately, there is no commercial entity that distributes thermoplastic nanofluidic devices at this writing in spite of the potential they can offer in the commercial market due to the ability to produce low-cost devices in a high production mode. For example, a cost assessment of micro/nano chip production using thermoplastics and replication-based production is shown in Table 4 (note that these costs do not include

overhead charges for commercialization and R&D operational costs). The low cost for production of thermoplastic devices compared to glass or silicon devices, and the high production rate[51,58] will assist in mitigating challenges currently seen in the nanofluidic market in terms of chip cost.

Conclusions

Nanofluidics is an emerging field offering unique processing capabilities not afforded when using microscale devices. Operating in the nanodomain allows for the interrogation of biopolymers at the single-molecule level, elongation of DNA for mapping or determining sequence specific variations, unique electrophoretic separations, and DNA/RNA sequencing. Because of these unique process capabilities enabling important applications for *in vitro* diagnostics, simple

Table 4 Cost analysis for device production of microfluidic and nanofluidic devices using a "cost of goods" analysis. Please note that these production costs do not include overhead charges or research & business development costs

Item	Microfluidics Cost/4″ chip [$]	Nanofluidics Cost/4″ chip [$]
Master mold[a]	0.10	3.00
Molding[b]	0.20	0.40
Post-processing[c]	0.25	0.25
Polymer substrate	0.25 (PMMA)	0.25 (PMMA)
Assembly[d]	1.05	3.20
Chemicals	0.20	0.50
Biologics	1.00	1.00
Electronic connects	0.85	3.55
Labor	1.10	2.50
Total cost per chip	5.00	14.65
Production rate[e]	150/day (8 h)	150/day (8 h)

Imprint Fluidic Structures

↓

Electronic Connections

↓

Cover Plate Assembly

↓

UV Activation and Biologics Immobilization
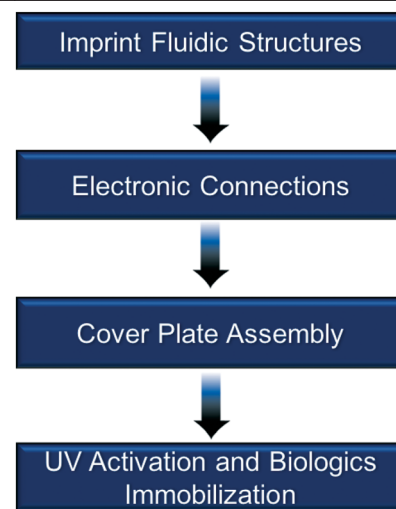
[a] Amortization for 1000 imprinting from single master and 20 polymer stamps. [b] Includes equipment amortization. [c] Cleaning of chip and activation for biologic attachment. [d] Includes cover plate material, equipment amortization for assembly. [e] The production rate is limited in both cases by the cycle time for the imprinting step for a single machine. Use of roll-to-roll imprinting will increase this production rate.

fabrication strategies of these devices that are conducive to high-scale production with high process yield rates must be realized to deliver devices appropriate for commercial translation.

This paper has presented an overview of recent advancements in the fabrication, assembly and surface modification/ characterization of thermoplastic nanofluidic devices as well as applications of such devices. Thermoplastics are particularly attractive substrates for nanofluidics because they are capable of being produced at high production rates and low-cost using established nanoscale replication techniques, such as NIL, roll imprinting or compression injection molding. In fact, the challenge with producing viable nanofluidic devices in thermoplastics is not necessarily the generation of nanostructures into the substrate, which typically involves a top-down approach, but assembly of devices without experiencing structural deformation of the patterned nanostructures. While several successful assembly strategies with high process yield rates were reviewed herein, techniques conducive to high scale production must be considered.

Another challenge with moving nanofluidic devices forward is careful control of the surface chemistry due to the extraordinary high surface-to-volume ratio associated with nanoslits or nanochannels and the fact that device performance is many times predicated on surface interactions. In addition, when using thermoplastic substrates that can possess a diverse range of hydrophobicities, viable surface modification protocols must be produced that can control the surface wettability of the device to allow for easy priming of the

fluidic nanochannels for EK pumping. The surface chemistry of thermoplastics is complicated because, unlike glass-based devices that are highly crystalline, polymers are amorphous creating disorganization in the spatial distribution of surface functional groups. This heterogeneous spatial distribution of functional groups can generate flow recirculation producing less than optimal performance, such as noted for nanoscale electrophoretic separations. However, the lower charge density on polymer surfaces compared to glass can reduce the consequences of this artifact and also, produce lower EOFs that can facilitate loading of charged analytes without concentration polarization effects.

Finally, the application portfolio of thermoplastic nanofluidic devices needs to be expanded. Much of the nanofluidic reports to-date and indeed, even the commercial venue for nanofluidic devices, have used glass-based devices mostly due to its well-established fabrication modalities and its well-defined surface chemistry. The question becomes: can tangible applications demonstrated in inorganic nanofluidic devices easily be transferred into thermoplastic nanofluidic devices? The answer is not a simple one because the assembly techniques are different and the surface chemistries are different. For example, surface activation of thermoplastics can be performed prior to assembly using UV/O$_3$ or O$_2$ plasma techniques to either increase the surface wettability of the substrate and/or produce surface functional groups. However, following thermal assembly near the T_g of the thermoplastic, many of these preformed functional groups can be buried within the bulk polymer. In addition, the use of organic solvents can be problematic

due to polymer dissolution and/or swelling making the device non-functional.

However, the evolution of nanofluidics is not so much different than microfluidics; most of the initial applications of microfluidics were entrenched in using glass type devices and has now evolved into a developmental phase where thermoplastics are becoming increasingly more popular due to the transition of microfluidics into the commercial sector and established production pipelines to generate devices at high scale and low cost, appropriate for *in vitro* diagnostics.

Acknowledgements

References

1 S. J. Kim, Y.-C. Wang, J. H. Lee, H. Jang and J. Han, *Phys. Rev. Lett.*, 2007, **99**, 044501.

2 R. K. Anand, E. Sheridan, K. N. Knust and R. M. Crooks, *Anal. Chem.*, 2011, **83**, 2351–2358.

3 A. Mani, T. A. Zangle and J. G. Santiago, *Langmuir*, 2009, **25**, 3898–3908.

4 A. Piruska, M. Gong, J. V. Sweedler and P. W. Bohn, *Chem. Soc. Rev.*, 2010, **39**, 1060–1072.

5 T. A. Zangle, A. Mani and J. G. Santiago, *Chem. Soc. Rev.*, 2010, **39**, 1014–1035.

6 E. B. Kalman, I. Vlassiouk and Z. S. Siwy, *Adv. Mater.*, 2008, **20**, 293–297.

7 R. B. Schoch, J. Han and P. Renaud, *Rev. Mod. Phys.*, 2008, **80**, 839–883.

8 J. W. van Honschoten, N. Brunets and N. R. Tas, *Chem. Soc. Rev.*, 2010, **39**, 1096–1114.

9 Y.-C. Wang, A. L. Stevens and J. Han, *Anal. Chem.*, 2005, **77**, 4293–4299.

10 S. J. Kim, L. D. Li and J. Han, *Langmuir*, 2009, **25**, 7759–7765.

11 Q. Pu, J. Yun, H. Temkin and S. Liu, *Nano Lett.*, 2004, **4**, 1099–1103.

12 A. Meller, L. Nivon, E. Brandin, J. Golovchenko and D. Branton, *Proc. Natl. Acad. Sci. U. S. A.*, 2000, **97**, 1079–1084.

13 D. Branton, D. W. Deamer, A. Marziali, H. Bayley, S. A. Benner, T. Butler, M. Di Ventra, S. Garaj, A. Hibbs, X. Huang, S. B. Jovanovich, P. S. Krstic, S. Lindsay, X. S. Ling, C. H. Mastrangelo, A. Meller, J. S. Oliver, Y. V. Pershin, J. M. Ramsey, R. Riehn, G. V. Soni, V. Tabard-Cossa, M. Wanunu, M. Wiggin and J. A. Schloss, *Nat. Biotechnol.*, 2008, **26**, 1146–1153.

14 M. Wanunu, W. Morrison, Y. Rabin, A. Y. Grosberg and A. Meller, *Nat. Nanotechnol.*, 2010, **5**, 160–165.

15 J. J. Kasianowicz, S. E. Henrickson, H. H. Weetall and B. Robertson, *Anal. Chem.*, 2001, **73**, 2268–2272.

16 B. M. Venkatesan and R. Bashir, *Nat. Nanotechnol.*, 2011, **6**, 615–624.

17 O. A. Saleh and L. L. Sohn, *Nano Lett.*, 2003, **3**, 37–38.

18 A. Mariam, I. Aleksandar, H. Jongin, K. Phillip, I. Emanuele, B. E. Joshua and A. Tim, *J. Phys.: Condens. Matter*, 2010, **22**, 454128.

19 J. Clarke, H.-C. Wu, L. Jayasinghe, A. Patel, S. Reid and H. Bayley, *Nat. Nanotechnol.*, 2009, **4**, 265–270.

20 S. W. Turner, M. Cabodi and H. G. Craighead, *Phys. Rev. Lett.*, 2002, **88**, 128103.

21 C. Danelon, C. Santschi, J. Brugger and H. Vogel, *Langmuir*, 2006, **22**, 10711–10715.

22 H. Craighead, *Nature*, 2006, **442**, 387–393.

23 H. G. Craighead, *J. Vac. Sci. Technol., A*, 2003, **21**, S216–S221.

24 L. D. Menard, C. E. Mair, M. E. Woodson, J. P. Alarie and J. M. Ramsey, *ACS Nano*, 2012, **6**, 9087–9094.

25 T. Tsukahara, K. Mawatari and T. Kitamori, *Chem. Soc. Rev.*, 2010, **39**, 1000–1013.

26 U. F. Keyser, S. van Dorp and S. G. Lemay, *Chem. Soc. Rev.*, 2010, **39**, 939–947.

27 S. Pennathur, F. Baldessari, J. G. Santiago, M. G. Kattah, J. B. Steinman and P. J. Utz, *Anal. Chem.*, 2007, **79**, 8316–8322.

28 L. D. Menard and J. M. Ramsey, *Anal. Chem.*, 2013, **85**, 1146–1153.

29 S. J. Kim, S. H. Ko, K. H. Kang and J. Han, *Nat. Nanotechnol.*, 2013, **8**, 609.

30 L.-J. Cheng and L. J. Guo, *Chem. Soc. Rev.*, 2010, **39**, 923–938.

31 F. Persson and J. O. Tegenfeldt, *Chem. Soc. Rev.*, 2010, **39**, 985–999.

32 X. Liang and S. Y. Chou, *Nano Lett.*, 2008, **8**, 1472–1476.

33 C. H. Reccius, J. T. Mannion, J. D. Cross and H. G. Craighead, *Phys. Rev. Lett.*, 2005, **95**, 268101.

34 S. L. Levy, J. T. Mannion, J. Cheng, C. H. Reccius and H. G. Craighead, *Nano Lett.*, 2008, **8**, 3839–3844.

35 S. L. Levy and H. G. Craighead, *Chem. Soc. Rev.*, 2010, **39**, 1133–1152.

36 H. Daiguji, *Chem. Soc. Rev.*, 2010, **39**, 901–911.

37 J. Han and H. G. Craighead, *Science*, 2000, **288**, 1026–1029.

38 L. A. Woods, P. U. Gandhi and A. G. Ewing, *Anal. Chem.*, 2005, **77**, 1819–1823.

39 H. Bayley and C. R. Martin, *Chem. Rev.*, 2000, **100**, 2575–2594.

40 P. J. Kemery, J. K. Steehler and P. W. Bohn, *Langmuir*, 1998, **14**, 2884–2889.

41 T.-C. Kuo, L. A. Sloan, J. V. Sweedler and P. W. Bohn, *Langmuir*, 2001, **17**, 6298–6303.

42 N. R. Tas, J. W. Berenschot, P. Mela, H. V. Jansen, M. Elwenspoek and A. van den Berg, *Nano Lett.*, 2002, **2**, 1031–1032.

43 L. D. Menard and J. M. Ramsey, *Nano Lett.*, 2011, **11**, 512–517.

44 V. Piotter, T. Hanemann, R. Ruprecht and J. Haußelt, *Microsyst. Technol.*, 1997, **3**, 129–133.

45 H. Becker and U. Heim, *Sens. Actuators, A*, 2000, **83**, 130–135.

46 M. Heckele and W. K. Schomburg, *J. Micromech. Microeng.*, 2004, **14**, R1.

47 P. Abgrall, L.-N. Low and N.-T. Nguyen, *Lab Chip*, 2007, **7**, 520–522.

48 H. Schift, C. David, M. Gabriel, J. Gobrecht, L. J. Heyderman, W. Kaiser, S. Köppel and L. Scandella, *Microelectron. Eng.*, 2000, **53**, 171–174.

49 P. Utko, F. Persson, A. Kristensen and N. B. Larsen, *Lab Chip*, 2011, **11**, 303–308.

50 X. Liang, K. J. Morton, R. H. Austin and S. Y. Chou, *Nano Lett.*, 2007, **7**, 3774–3780.

51 R. Chantiwas, M. L. Hupert, S. R. Pullagurla, S. Balamurugan, J. Tamarit-Lopez, S. Park, P. Datta, J. Goettert, Y.-K. Cho and S. A. Soper, *Lab Chip*, 2010, **10**, 3255–3264.

52 J. O. Tegenfeldt, C. Prinz, H. Cao, R. L. Huang, R. H. Austin, S. Y. Chou, E. C. Cox and J. C. Sturm, *Anal. Bioanal. Chem.*, 2004, **378**, 1678–1692.

53 Q. Xia, K. J. Morton, R. H. Austin and S. Y. Chou, *Nano Lett.*, 2008, **8**, 3830–3833.

54 S. A. Soper, A. C. Henry, B. Vaidya, M. Galloway, M. Wabuyele and R. L. McCarley, *Anal. Chim. Acta*, 2002, **470**, 87–99.

55 S. B. Hawthorne, Y. Yang, C. B. Grabanski, D. J. Miller and M. L. Lee, *Anal. Chem.*, 2000, **72**, 642–643.

56 S. L. Llopis, J. Osiri and S. A. Soper, *Electrophoresis*, 2007, **28**, 984–993.

57 J. M. Jackson, M. A. Witek, M. L. Hupert, C. Brady, S. Pullagurla, J. Kamande, R. D. Aufforth, C. J. Tignanelli, R. J. Torphy, J. J. Yeh and S. A. Soper, *Lab Chip*, 2014, **14**, 106–117.

58 A. C. Henry, T. J. Tutt, M. Galloway, Y. Y. Davidson, C. S. McWhorter, S. A. Soper and R. L. McCarley, *Anal. Chem.*, 2000, **72**, 5331–5337.

59 P. Abgrall and N. T. Nguyen, *Anal. Chem.*, 2008, **80**, 2326–2341.

60 M. Gad-el-Hak, *J. Fluids Eng.*, 1999, **121**, 5–33.

61 A. T. Conlisk, *Electrophoresis*, 2005, **26**, 1896–1912.

62 Z. Yuan, A. L. Garcia, G. P. Lopez and D. N. Petsev, *Electrophoresis*, 2007, **28**, 595–610.

63 S. Pennathur and J. Santiago, *Anal. Chem.*, 2005, **77**, 6772–6781.

64 F. Baldessari and J. Santiago, *J. Nanobiotechnol.*, 2006, **4**, 12.

65 S. Movahed and D. Li, *Electrophoresis*, 2011, **32**, 1259–1267.

66 X. L. Xuan and D. Li, *Electrophoresis*, 2006, **27**, 5020–5031.

67 C. E. O'Neil, J. M. Jackson, S.-H. Shim and S. A. Soper, *Anal. Chem.*, 2016, **88**(7), 3686–3696.

68 N. Kaji, R. Ogawa, A. Oki, Y. Horiike, M. Tokeshi and Y. Baba, *Anal. Bioanal. Electrochem.*, 2006, **386**, 759–764.

69 W. Moran, C. Chi-Chang and R.-J. Yang, *J. Chem. Phys.*, 2010, **132**, 024701.

70 F. I. Uba, S. Pullagurla, N. Sirasunthorn, J. Wu, S. Park, R. Chantiwas, Y.-K. Cho, H. Shin and S. A. Soper, *Analyst*, 2015, **140**, 113–126.

71 B. R. Novak, D. Moldovan, D. E. Nikitopoulos and S. A. Soper, *J. Phys. Chem. B*, 2013, **117**, 3271–3279.

72 K. Xia, B. R. Novak, K. M. Weerakoon-Ratnayake, S. A. Soper, D. E. Nikitopoulos and D. Moldovan, *J. Phys. Chem. B*, 2015, **119**, 11443–11458.

73 R. Carr, J. Comer, M. D. Ginsberg and A. Aksimentiev, *Lab Chip*, 2011, **11**, 3766–3773.

74 D. Xia, J. Yan and S. Hou, *Small*, 2012, **8**, 2787–2801.

75 A. de la Escosura-Muñiz and A. Merkoçi, *ACS Nano*, 2012, **6**, 7556–7583.

76 R. Chantiwas, S. Park, S. A. Soper, B. C. Kim, S. Takayama, V. Sunkara, H. Hwang and Y.-K. Cho, *Chem. Soc. Rev.*, 2011, **40**, 3677–3702.

77 N. Douville, D. Huh and S. Takayama, *Anal. Bioanal. Chem.*, 2008, **391**, 2395–2409.

78 D. Mijatovic, J. C. T. Eijkel and A. van den Berg, *Lab Chip*, 2005, **5**, 492–500.

79 C. Duan, W. Wang and Q. Xie, *Biomicrofluidics*, 2013, 7, 026501.

80 J. O. Tegenfeldt, C. Prinz, H. Cao, S. Chou, W. W. Reisner, R. Riehn, Y. M. Wang, E. C. Cox, J. C. Sturm, P. Silberzan and R. H. Austin, *Proc. Natl. Acad. Sci. U. S. A.*, 2004, **101**, 10979–10983.

81 M. Cabodi, S. W. P. Turner and H. G. Craighead, *Anal. Chem.*, 2002, **74**, 5169–5174.

82 C. Kyo Seon, K. Seungwook, C. Haegeun, O. Joon-Ho, S. Tae-Yeon, A. Boo Hyun, K. Young Keun, P. Jae Hyoung, D. Young Rag and K. Woong, *Nanotechnology*, 2010, **21**, 425302.

83 S. Tan, K. Klein, D. Shima, R. Livengood, E. Mutunga and A. Vladar, *J. Vac. Sci. Technol., B: Nanotechnol. Microelectron.: Mater., Process., Meas., Phenom.*, 2014, **32**, 06FA01.

84 J. Yang, D. C. Ferranti, L. A. Stern, C. A. Sanford, J. Huang, Z. Ren, L.-C. Qin and A. R. Hall, *Nanotechnology*, 2011, **22**, 285310.

85 F. I. Uba, B. Hu, K. Weerakoon-Ratnayake, N. Oliver-Calixte and S. A. Soper, *Lab Chip*, 2015, **15**, 1038–1049.

86 S. Y. Chou, P. R. Krauss and P. J. Renstrom, *Appl. Phys. Lett.*, 1995, **67**, 3114–3116.

87 S. Y. Chou, P. R. Krauss and P. J. Renstrom, *J. Vac. Sci. Technol., B: Microelectron. Nanometer Struct.–Process., Meas., Phenom.*, 1996, **14**, 4129–4133.

88 S. Y. Chou and P. R. Krauss, *Microelectron. Eng.*, 1997, **35**, 237–240.

89 P. E. Shao, A. van Kan, L. P. Wang, K. Ansari, A. A. Bettiol and F. Watt, *Appl. Phys. Lett.*, 2006, **88**, 093515.

90 P. Sivanesan, K. Okamoto, D. English, C. S. Lee and D. L. DeVoe, *Anal. Chem.*, 2005, **77**, 2252–2258.

91 J.-M. Li, C. Liu, X. Ke, Y.-J. Duan, Y. Fan, M. Li, K.-P. Zhang, Z. Xu and L.-D. Wang, *Microsyst. Technol.*, 2013, **19**, 1845–1850.

92 E. Cheng, H. Zou, Z. Yin, P. Jurcicek and X. Zhang, *J. Micromech. Microeng.*, 2013, **23**(7), 075022.

93 L. Junshan, Q. Hongchao, X. Zheng, L. Chong, W. Junyao, D. Liqun, Z. Xi and W. Liding, *Micro Nano Lett.*, 2012, **7**, 159–162.

94 J. Liu, X. Jin, T. Sun, Z. Xu, C. Liu, J. Wang, L. Chen and L. Wang, *Microsyst. Technol.*, 2013, **19**, 629–634.

95 J.-M. Li, C. Liu, X. Ke, Z. Xu, Y.-J. Duan, Y. Fan, M. Li, K.-P. Zhang and L.-D. Wang, *Lab Chip*, 2012, **12**, 4059–4062.

96 L. Zhang, F. Gu, L. Tong and X. Yin, *Microfluid. Nanofluid.*, 2008, **5**, 727–732.

97 J. Wu, R. Chantiwas, A. Amirsadeghi, S. A. Soper and S. Park, *Lab Chip*, 2011, **11**, 2984–2989.

98 C.-W. Tsao and D. DeVoe, *Microfluid. Nanofluid.*, 2009, **6**, 1–16.

99 S.-J. Hwang, M.-C. Tseng, J.-R. Shu and H. Her Yu, *Surf. Coat. Technol.*, 2008, **202**, 3669–3674.

100 S. Roy and C. Y. Yue, *Plasma Processes Polym.*, 2011, **8**, 432–443.

101 H. T. Lasse, K. Anna and K. Anders, *Nanotechnology*, 2008, **19**, 125301.

102 C. E. O'Neil, S. Taylor, K. Ratnayake, S. Pullagurla, V. Singh and S. A. Soper, *Analyst*, 2016, **141**, 6521–6532.

103 Y. H. Cho, J. Park, H. Park, X. Cheng, B. J. Kim and A. Han, *Microfluid. Nanofluid.*, 2010, **9**, 163–170.

104 X. Hu, Q. He, X. Zhang and H. Chen, *Microfluid. Nanofluid.*, 2011, **10**, 1223–1232.

105 A. Piruska, I. Nikcevic, S. H. Lee, C. Ahn, W. R. Heineman, P. A. Limbach and C. J. Seliskar, *Lab Chip*, 2005, **5**, 1348–1354.

106 G. Khanarian and H. Celanese, *Opt. Eng.*, 2001, **40**, 1024–1029.

107 R. B. Schoch and P. Renaud, *Appl. Phys. Lett.*, 2005, **86**, 25311–25313.

108 D. C. Martins, V. Chu and J. P. Conde, *Biomicrofluidics*, 2013, **7**(034111), 1–21.

109 D. Stein, M. Kruithof and C. Dekker, *Phys. Rev. Lett.*, 2004, **93**, 035901.

110 S. Roy, C. Y. Yue, Y. C. Lam, Z. Y. Wang and H. Hu, *Sens. Actuators, B*, 2010, **150**, 537–549.

111 A. Vesel and M. Mozetic, *Vacuum*, 2012, **86**, 634–637.

112 X. Huang, M. J. Gordon and R. N. Zare, *Anal. Chem.*, 1988, **60**, 1837–1838.

113 J. T. Mannion, C. H. Reccius, J. D. Cross and H. G. Craighead, *Biophys. J.*, 2006, **90**, 4538–4545.

114 H. Cao, J. O. Tegenfeldt, R. H. Austin and S. Y. Chou, *Appl. Phys. Lett.*, 2002, **81**, 3058–3060.

115 W. Reisner, K. J. Morton, R. Riehn, Y. M. Wang, Z. Yu, M. Rosen, J. C. Sturm, S. Y. Chou, E. Frey and R. H. Austin, *Phys. Rev. Lett.*, 2005, **94**, 196101.

116 G. S. Manning, *Biophys. J.*, 2006, **91**, 3607–3616.

117 H. Orland, *J. Phys. I*, 1994, **4**, 101–114.

118 A. Baumgärtner, *Polymer*, 1982, **23**, 334–335.

119 D. W. Schaefer, J. F. Joanny and P. Pincus, *Macromolecules*, 1980, **13**, 1280–1289.

120 W. Reisner, J. P. Beech, N. B. Larsen, H. Flyvbjerg, A. Kristensen and J. O. Tegenfeldt, *Phys. Rev. Lett.*, 2007, **99**(5), 058302.

121 B. Chu, *J. Am. Chem. Soc.*, 1983, **105**, 5169–5169.

122 T. Odijk, *J. Chem. Phys.*, 2006, **125**, 204904.

123 T. Odijk, *Macromolecules*, 1983, **16**, 1340–1344.

124 R. Walter, N. P. Jonas and H. A. Robert, *Rep. Prog. Phys.*, 2012, **75**, 106601.

125 L. Dai, J. van der Maarel and P. S. Doyle, *Macromolecules*, 2014, **47**, 2445–2450.

126 L. J. Guo, X. Cheng and C.-F. Chou, *Nano Lett.*, 2003, **4**, 69–73.

127 L. H. Thamdrup, A. Klukowska and A. Kristensen, *Nanotechnology*, 2008, **19**, 125301.

128 Y. Michaeli and Y. Ebenstein, *Nat. Biotechnol.*, 2012, **30**, 762–763.

129 M. Levy-Sakin and Y. Ebenstein, *Curr. Opin. Biotechnol.*, 2013, **24**, 690–698.

130 E. T. Lam, A. Hastie, C. Lin, D. Ehrlich, S. K. Das, M. D. Austin, P. Deshpande, H. Cao, N. Nagarajan, M. Xiao and P.-Y. Kwok, *Nat. Biotechnol.*, 2012, **30**, 771–776.

131 H. Cao, A. R. Hastie, D. Cao, E. T. Lam, Y. Sun, H. Huang, X. Liu, L. Lin, W. Andrews and S. Chan, *GigaScience*, 2014, **3**, 1–11.

132 S. K. Das, M. D. Austin, M. C. Akana, P. Deshpande, H. Cao and M. Xiao, *Nucleic Acids Res.*, 2010, **38**, e177.

133 H. Shadpour, H. Musyimi, J. Chen and S. A. Soper, *J. Chromatogr. A*, 2006, **1111**, 238–251.

134 K. M. Weerakoon-Ratnayake, F. I. Uba, N. J. Oliver-Calixte and S. A. Soper, *Anal. Chem.*, 2016, **88**(7), 3569–3577.

135 N. J. Oliver-Calixte, F. I. Uba, K. N. Battle, K. M. Weerakoon-Ratnayake and S. A. Soper, *Anal. Chem.*, 2014, **86**, 4447–4454.

136 J. Liu, L. Wang, W. Ouyang, W. Wang, J. Qin, Z. Xu, S. Xu, D. Ge, L. Wang and C. Liu, *Biosens. Bioelectron.*, 2015, **72**, 288–293.

137 C. Wang, D.-K. Ye, Y.-Y. Wang, T. Lu and X.-H. Xia, *Lab Chip*, 2013, **13**, 1546–1553.

138 S. Y. Yang, S. Son, S. Jang, H. Kim, G. Jeon, W. J. Kim and J. K. Kim, *Nano Lett.*, 2011, **11**, 1032–1035.

139 M. G. Knepley, D. A. Karpeev, S. Davidovits, R. S. Eisenberg and D. Gillespie, *J. Chem. Phys.*, 2010, **132**, 124101.

140 R. H. Nilson and S. K. Griffiths, *J. Chem. Phys.*, 2006, **125**, 164510.

141 BioNanoGenomics, *Assembling high-quality human genomes – Beyond the '$1,000 genome'*, PacBio Literature, 2015.

142 BioNanoGenomics, BioNano Genomics.Inc, San Diego, CA, 2015.

143 S. R.-. GenomeWeb, Oxford Nanopore Releases Pricing for MinIon Flow Cells as Users Publish New Data, Applications, https://www.genomeweb.com/sequencing-technology/oxford-nanopore-releases-pricing-minion-flow-cells-users-publish-new-data, Accessed November 17, 2016.